Liver International 2006; 26: 986–993

Liver International
DOI: 10.1111/j.1478-3231.2006.01317.x

Basic Studies

IFNγ expression inhibits LHBs storage disease and ground glass hepatocyte appearance, but exacerbates inflammation and apoptosis in HBV surface protein-accumulating transgenic livers

Reifenberg K, Hildt E, Lecher B, Wiese E, Nusser P, Ott S, Yamamura K-I, Rutter G, Löhler J. IFNγ expression inhibits LHBs storage disease and ground glass hepatocyte appearance, but exacerbates inflammation and apoptosis in HBV surface protein accumulating transgenic livers. Liver International 2006: 26: 986–993.

Abstract: *Background/Aims:* Interferon γ (IFNγ) controls hepatitis B virus replication. As systemic application may cause severe adverse effects, approaches of liver-directed IFNγ gene therapy may represent an attractive alternative for treatment of chronic viral hepatitis B and thus needs testing *in vivo* in suitable animal models. *Methods:* We therefore crossbred Alb-1HBV transgenic mice overexpressing the large HBV surface protein (LHBs) in their livers and developing LHBs storage disease and ground glass hepatocyte appearance with SAP-IFNγ transgenic animals previously shown to exhibit constitutive hepatic IFNγ expression, and analyzed the resulting double-transgenic offspring. *Results:* We found that IFNγ coexpression significantly reduced hepatic LHBs expression and thereby inhibited hepatocellular LHBs storage disease and ground glass hepatocyte appearance. The beneficial antiviral IFNγ effects as observed in Alb1-HBV SAP-IFNγ double-transgenic livers were associated with significantly elevated serum ALT concentrations, massive mononuclear cell infiltrates, appearance of Councilman bodies, and increased α-PARP (poly(ADP-ribose) polymerase cleavage). *Conclusions:* Exacerbation of hepatic necroinflammation and increased hepatocellular apoptosis rate in IFNγ-expressing Alb1-HBV transgenic livers suggest that special precautions be taken for testing approaches of liver-specific IFNγ expression in patients with chronic hepatitis B.

Kurt Reifenberg[1], Eberhard Hildt[2], Bernd Lecher[1], Elena Wiese[1], Petra Nusser[3], Sibylle Ott[3], Ken-Ichi Yamamura[4], Gabriel Rutter[5] and Jürgen Löhler[5]

[1]Central Laboratory Animal Facility, University of Mainz, Mainz, Germany, [2]Robert Koch Institut, Berlin, Germany, [3]Laboratory Animal Research Unit, University of Ulm, Ulm, Germany, [4]Institute of Molecular Embryology and Genetics, Kumamoto, Japan and [5]Heinrich Pette Institute for Experimental Virology and Immunology, Hamburg, Germany

Key words: chronic hepatitis B – ground glass hepatocyte – hepatitis B virus – interferon-γ – LHBs storage – transgenic mice

Kurt Reifenberg, Central Laboratory Animal Facility, University of Mainz, Obere Zahlbacherstr. 67 – Hochhaus Augustusplatz, D-55131 Mainz, Germany.
Tel: +49 6131 39 33125
Fax: +49 6131 39 30220
e-mail: reifenbe@uni-mainz.de

Received 4 April 2006,
accepted 22 May 2006

The hepatitis B virus (HBV) causes acute and chronic liver inflammation and it is generally accepted that persistent HBV infection is caused by an inadequate immune response, which is insufficient to control viral replication but vigorous enough to induce continuous hepatic necroinflammation (1). Chronic courses of HBV infection are of major epidemiological importance because of the frequent complication of disease by liver cirrhosis and hepatocellular carcinoma (2). Hepatocytes with a characteristic glassy or ground glass appearance represent a characteristic clinical hallmark of chronic hepatitis B. Such ground glass hepatocytes result from abundant deposition of the large hepatitis B virus surface antigen (LHBs) in the hepatocellular endoplasmic reticulum (3–9); however, the precise mechanism leading to LHBs storage disease in chronic HBV patients is unknown (10–12). Alb-1HBV transgenic mice (13, 14) carry the pre-S1, pre-S2, and S regions of the HBV surface open reading frame cloned downstream of the murine albumine promoter and thus overexpress the LHBs protein. The LHBs filaments of Alb-1HBV transgenic hepatocytes are abundantly deposited in the endoplasmatic reticulum, leading

to storage disease and massive appearance of ground glass hepatocytes. Alb1-HBV transgenic mice show a chronic progressive hepatitis that culminates in the development of hepatic adenomas and carcinomas (13–20) and thus represent an important *in vivo* model for the chronic HBV carrier state.

So far, no efficient therapy of chronic hepatitis B is available. In recent studies, it was suggested that the cytokines interferon γ (IFNγ), tumor necrosis factor α (TNFα), interleukin-12, and interleukin-18 play an important role in the control of HBV gene expression. The mechanisms underlying the antiviral effects of proinflammatory cytokines were found to operate at the transcriptional and post-transcriptional level and did not imply cytopathic effects (21–27) rendering these cytokines interesting candidates for the treatment of chronic hepatitis B. So far, clinical use of proinflammatory cytokines was strongly restricted due to potential toxicity resulting from systemic application. However, new therapeutic approaches like liver-directed gene therapy (28) or locoregional immunochemotherapy (29) may be suited to overcome such a problem. Thus, there is an urgent need to test the promising anti-hepadnaviral applications of proinflammatory cytokines in suitable animal models.

The aim of the present study was to investigate the effects of a liver-specific expression of the proinflammatory cytokine IFNγ on LHBs accumulation and on ground glass hepatocyte morphology. To this end, Alb1-HBV mice were crossbred with transgenic animals previously shown to express IFNγ constitutively in their livers (30), and the hepatic phenotype of the resulting double-transgenic offspring was analyzed. We found that constitutive hepatic IFNγ coexpression had the potential to reduce hepadnaviral surface gene expression significantly and thus to inhibit ground glass hepatocyte appearance. However, the beneficial antiviral IFNγ effects were associated with an exacerbation of hepatic inflammation and abundant hepatocellular apoptosis.

Materials and methods

Transgenic mice

Transgenic mice were maintained at the Laboratory Animal Research Unit of the University of Ulm or the Central Laboratory Animal Facility of Mainz under specified pathogen-free conditions. The mice received humane care, and all experiments were approved by the local authorities.

Generation and characteristics of transgenic lineages Tg(Alb-1HBV)Bri44 (13–20), internal designation (Alb-1HBV), and SAP-IFNγ5 (30, internal designation: SAP-IFNγ) have been described previously. Briefly, Alb-1HBV transgenic mice carry the entire HBV surface open reading frame downstream of the murine albumine promoter and SAP-IFNγ5 transgenic animals harbor the cDNA of the murine IFNγ gene under the transcriptional regulation of the liver-specific promoter of the human serum amyloid P component gene.

The Alb-1HBV and SAP-IFNγ5 strains used in the present study had an inbred C57BL/6 (B6) genetic background and were propagated by crossing hemizygous transgenic males to B6 females. Alb-1HBV-transgenic individuals were discriminated from their nontransgenic littermates by PCR amplification of transgene-specific sequences using primers 5′-CAG TGG AAT TCC ACA ACC-3′ and 5′-AGA AAA ACC CCG CCT GTA-3′. SAP-IFNγ mice were genotyped by using primers 5′-TCA CCA CTC CTT ACC GTA-3′ and 5′-GAA GAG CTG CAA AGC CAA-3′. Alb-1HBV SAP-IFNγ double-transgenic mice were generated by crossbreeding hemizygous Alb-1HBV females with SAP-IFNγ males.

RNA analyses

RNA analyses were performed as described previously (31, 32). Briefly, total liver RNA was obtained by the RNEasy Midi Kit (Quiagen, Hilden, Germany). Hepatic expression of the IFNγ transgene was analyzed by using a semiquantitative RT-PCR protocol implying reverse transcription (Superscript TM II, Gibco BRL, Gaithersburg, MD, USA) of 2.5 µg of total RNA with an oligo-(dT)-based primer and consecutive PCR reactions using the IFNγ-specific primers 5′-GAA AGC CTA GAA AGT CTG AAT AAC T-3′ and 5′-ATC AGC AGC GAC TCC TTT TCC GCT T-3′ (33). A GAPDH-specific RT-PCR reaction using primers 5′-ATG GTG AAG GTC GGT GTG AAC G-3′ and 5′-GTT GTC ATG GAT GAC CTT GGC C-3′ (33) was performed for RNA equilibration. For Northern blotting, 15 µg of total liver RNA was separated on an agarose/formaldehyde gel and subsequently blotted onto nylon membranes. The membranes were hybridized with an HBV- or GAPDH-specific ^{32}P-labelled probe, respectively.

Western blotting

Gels were loaded with 20 µg total liver protein per lane. SDS-PAGE was performed according to the

method of Laemmli. Before loading, samples were adjusted to identical protein concentrations. For Western blot analysis, poly(ADP-ribose) polymerase (α-PARP)-, actin-, and PCNA-specific sera (Santa Cruz Biotechnology, Santa Cruz, CA, USA) were used.

Histology

Liver samples were fixed in 4% buffered formaldehyde solution and slides were stained with hematoxylin and eosin according to standard protocols. For quantification of mononuclear infiltrate, five representative liver slides were investigated per mouse. Randomly selected slide regions were photographed and the percentage of infiltrate area was calculated in relation to the total area investigated.

Immunohistology and ultrastructural investigations

HBsAg and PCNA immunostaining was performed with paraffin sections using the avidin–biotin complex method. Sections were treated with 0.01 M citrate buffer (pH 6.0) in a microwave oven or a commercial 'target unmasking fluid' (Dianova, Hamburg, Germany) before antibody incubation. The sections were incubated overnight at 4 °C with a 1:3000 diluted polyclonal rabbit antiserum specific for all HBV surface gene products (generously provided by Reinhold Schirmbeck, University of Ulm, Germany) or PCNA. Specifically bound antibody was detected with a biotinylated secondary antibody and subsequent incubation with a streptavidin-labelled peroxidase complex (DAKO Diagnostika, Hamburg, Germany) or phosphatase-conjugated extravidin and staining with 3,3-diaminobenzidine tetrahydrochloride and naphthol AS-BI phosphate in combination with hexazotized new fuchsine (Merck, Darmstadt, Germany), respectively. Ultrastructural analyses and immunogold staining were performed as described previously (34).

Serum alanine transaminase (ALT) determination

ALT was quantitated in murine serum using the Reflotron system (Praemix, Mannheim, Germany).

Statistical analysis

T-tests were used to compare serum ALT and IFNγ concentrations as well as hepatic mononuclear infiltrates.

Results

Hepatic IFNγ coexpression in Alb-1HBV transgenic mice.

As shown previously, LHBs accumulating Alb-1HBV transgenic hepatocytes exhibit an extraordinary susceptibility to IFNγ-mediated cytotoxicity (35, 36). Thus it could not be excluded that hepatic IFNγ coexpression might lead to pre- or perinatal death of Alb-1HBV transgenic mice. However, upon genotyping of the juvenile Alb-1HBV × SAP-IFNγ offspring mice inheritance of the Alb-1HBV and SAP-IFNγ transgenes was found to be according to Mendelian rules (data not shown). Further, the Alb-1HBV SAP-IFNγ double-transgenic mice as well as their single- and nontransgenic littermates showed a normal development up to an age of about 6 months. Only at later age levels did the Alb-1HBV SAP-IFNγ double-transgenic as well as the SAP-IFNγ single-transgenic animals show a significantly increased mortality (data not shown). Owing to this experimental restriction, we confined our study to a maximum murine age level of 6 months.

To control for the normal expression of the SAP-IFNγ transgene, we performed RT-PCR analyses using transgenic liver RNA and additionally determined murine IFNγ serum concentrations. As shown in Fig. 1A, a high-level hepatic IFNγ transcription could be observed in the Alb-1HBV SAP-IFNγ double-transgenic as well as SAP-IFNγ single-transgenic mice, whereas virtually no liver-specific cytokine transcription was detectable in the Alb-1HBV and nontransgenic control animals. In line with this result, we found high IFNγ serum levels in 6-month-old Alb-1HBV SAP-IFNγ double-transgenic (mean of three animals: 12.5 U/ml, standard deviation: 6.6 U/ml) and SAP-IFNγ single-transgenic (mean of four animals: 15.7 U/ml, standard deviation: 22.2 U/ml) mice. In contrast, no IFNγ serum expression could be observed in Alb1-HBV single-transgenic and nontransgenic controls (data not shown). The SAP-IFNγ transgene could thus efficiently be expressed in LHBs accumulating Alb1-HBV transgenic mice.

Reduction of HBV surface gene expression by IFNγ

In our next experiment, we analyzed the influence of IFNγ coexpression on hepadnaviral gene expression using Northern blot technology. As illustrated in Fig. 1A, expression of all HBV surface gene transcripts was significantly reduced in the livers of double-transgenic Alb-1HBV SAP-IFNγ mice as compared with age-matched Alb-1HBV single-transgenic controls. To investi-

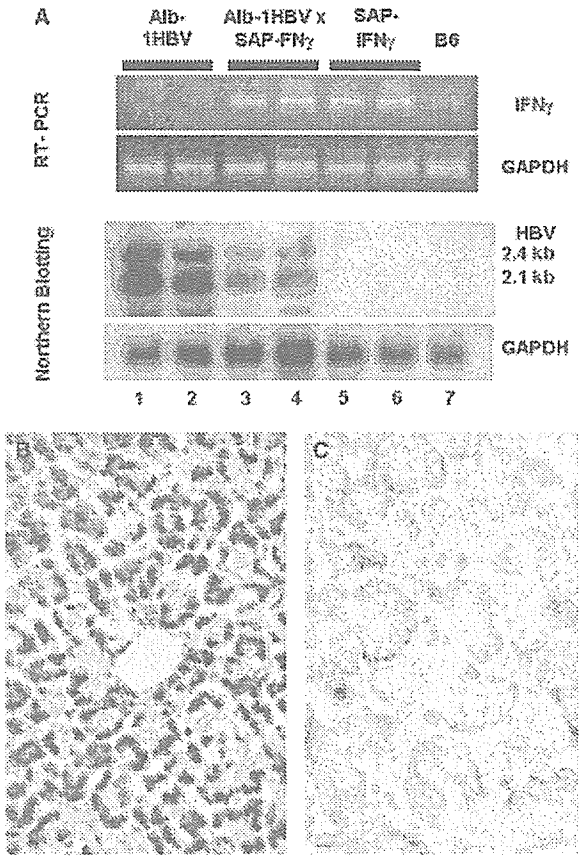

Fig. 1. Impairment of hepatitis B virus (HBV) surface gene expression by interferon γ (IFNγ) coexpression. (A) Total liver RNA was prepared from 2-month-old Alb-1HBV single-transgenic (lanes 1 and 2), Alb-1HBV SAP-IFNγ double-transgenic (lanes 3 and 4), SAP-IFNγ single-transgenic (lanes 5 and 6), and non-transgenic mice (lane 7). The RNAs were subjected to RT-PCR analyses using IFNγ- and GAPDH-specific primers at 35 and 25 cycles of amplification, respectively. Note that intensive IFNγ-specific RT-PCR signals could only be detected in Alb-1HBV SAP-IFNγ double-transgenic (lanes 3 and 4) and SAP-IFNγ single-transgenic (lanes 5 and 6) livers, indicating the suitability of the SAP-IFNγ transgene to express IFNγ efficiently in murine livers. Northern blots were hybridized with a P^{32}-labelled HBV-specific probe. Note the significant reduction of hepatic expression of the 2.4 kb LHBs-specific transcript and of the 2.1 kb middle and small HBs-specific transcripts in the Alb-1HBV SAP-IFNγ double-transgenic mice (lanes 3 and 4) as compared with the Alb-1HBV single-transgenic controls (lanes 1 and 2). A GAPDH-specific hybridization reaction was used to equilibrate the HBV-specific Northern blot. (B, C) Liver sections of Alb-1HBV single-transgenic (B) and Alb-1HBV SAP-IFNγ double-transgenic (C) mice were stained with a polyclonal antibody recognizing all HBV surface gene products. Note the significant reduction of total staining intensity and the modified staining pattern in double-transgenic livers (C) as compared with single-transgenic controls (B). Negative controls implied liver sections of SAP-IFNγ single-transgenic and non-transgenic animals (data not shown).

gate whether the significant reduction of HBV surface gene transcription as induced by IFNγ could also be confirmed at the protein level, we performed an immunohistological analysis. As depicted in Fig. 1, HBV surface protein-specific staining intensity was significantly reduced in Alb-1HBV SAP-IFNγ double-transgenic livers (Fig. 1C) as compared with the Alb-1HBV single-transgenic controls (Fig. 1B). In addition, the subcellular HBsAg distribution pattern of double-transgenic hepatocytes differed from that of the single-transgenic counterparts. Whereas the Alb-1HBV single-transgenic hepatocytes showed an intensive and homogenous cytoplasmic staining reaction (Fig. 1B), the Alb-1HBV SAP-IFNγ double-transgenic hepatocytes (Fig. 1C) exhibited a more diffuse staining pattern that was characterized by preferential staining of the peripheral cellular regions.

Normalization of ground glass morphology and storage disease by IFNγ coexpression

In the following, we analyzed by histology whether the significant reduction of LHBs protein expression as mediated by IFNγ had the potential to modify the ground glass hepatocyte appearance characteristic for Alb1-HBV transgenic mice (Fig. 2A, 15). We found that no significant numbers of ground glass hepatocytes could be detected in any double-transgenic liver (Fig. 2B).

To further investigate this IFNγ effect, we performed ultrastructural analyses with Alb-1HBV single-transgenic and Alb-1HBV SAP-IFNγ double-transgenic liver slides. As expected (15), a massive deposition of filaments (Fig. 2C) could be detected in the endoplasmatic reticulum (ER) of Alb-1HBV single-transgenic hepatocytes. These filaments showed a positive reaction in an immunogold staining using an HBsAg-specific antibody (Fig. 2C, inset) clearly indicating their LHBs composition. In stark contrast, the ER of Alb-1HBV SAP-IFNγ double-transgenic hepatocytes was virtually free of LHBs filament storage (Fig. 2D).

Thus, IFNγ had the potential to inhibit LHBs storage disease and ground glass hepatocyte appearance in Alb1-HBV mice.

IFNγ-mediated exacerbation of Alb1-HBV hepatitis

Juvenile Alb-1HBV single-transgenic mice only show minor signs of hepatic inflammation characterized by discrete mononuclear infiltrates and slightly elevated transaminase serum levels (16). To investigate whether coexpression of the proinflammatory cytokine IFNγ might exacerbate Alb-1HBV hepatitis, we determined serum ALT concentrations in the offspring mice of the Alb-1HBV × SAP-IFNγ cross. As demonstrated in Fig. 3, the Alb-1HBV and SAP-IFNγ single-transgenic mice only displayed a minor elevation

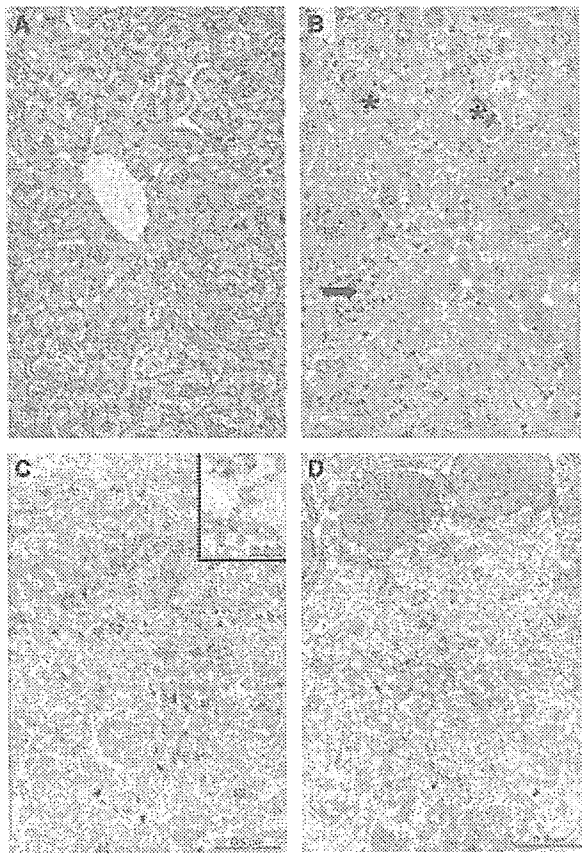

Fig. 2. (A, B) Inhibition of ground glass hepatocyte appearance by interferon γ (IFNγ). Liver slides of 6 months old Alb-1HBV single-transgenic (A) and Alb-1HBV × SAP-IFNγ double-transgenic (B) mice were analyzed by histology. In the Alb-1HBV single-transgenic livers (A), most hepatocytes exhibited cytoplasmatic inclusions composed of a fine-granular, slighly eosinophilic material characteristic for the ground glass hepatocyte appearance typically associated with chronic HBV. Only minor inflammatory infiltrates and no signs of hepatocellular apoptosis (Councilman bodies) could be detected in the liver parenchyma of the Alb-1HBV single-transgenic animal. In contrast, the Alb-1HBV SAP-IFNγ double-transgenic livers (B) lacked ground glass hepatocyte appearance (no significant numbers of ground glass hepatocytes detectable in at least 10 double-transgenic mice) but exhibited strong inflammatory reactions characterized by mononuclear infiltrates (arrow). Note the Councilman bodies (asterisks) in the Alb-1HBV SAP-IFNγ double-transgenic liver indicative of vigorous hepatocellular apoptosis. Minor signs of hepatic infiltration and no ground glass hepatocytes could be detected in the liver sections of the SAP-IFNγ single-transgenic transgenic mice and the livers of non-transgenic mice showed a normal phenotype (data not shown). The pictures shown represent HE stains and are typical for the respective murine genotype. (C, D) Reduction of large HBV surface protein (LHBs) storage disease by IFNγ coexpression. Hepatocytes of 6-month-old Alb-1HBV single-transgenic (C) and Alb-1HBV SAP-IFNγ double-transgenic (D) mice were subjected to ultrastructural analyses. Single-transgenic hepatocytes exhibited extensive accumulation of filaments in the extended cisterns of the ER, resulting in excessive formation of vacuoles (C, arrowheads). The filamentous material showed a positive reaction in an immunogold staining reaction performed with an HBsAg-specific antibody (C, inset). In contrast, the ER of Alb-1HBV SAP-IFNγ double-transgenic hepatocytes was free of LHBs filament storage (D, arrows), and LHBs accumulation was restricted to a few ER profiles (D, arrowheads). HBV, hepatitis B virus.

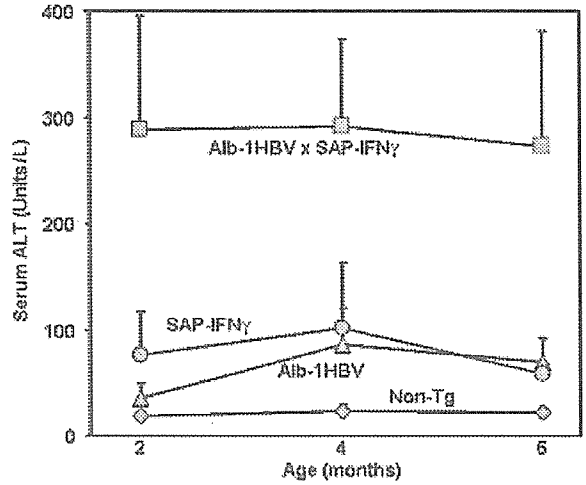

Fig. 3. Significant exacerbation of hepatitis in Alb1-HBV transgenic livers by interferon γ (IFNγ) coexpression. Serum samples of SAP-IFNγ Alb-1HBV double-transgenic (■), Alb-1HBV single-transgenic (▲), SAP-IFNγ single-transgenic (●), and non-transgenic (◆) mice were obtained at an age of 2, 4, and 6 months and the alanine aminotransferase (ALT) concentrations were determined. Serum ALT levels of Alb-1HBV and SAP-IFNγ single-transgenic mice were only slightly elevated as compared with those of non-transgenic control animals. In contrast, the serum ALT concentrations of the Alb-1HBV SAP-IFNγ double-transgenic mice were significantly (*T*-test, $P<0.05$) increased as compared with the single- and non-transgenic counterparts. Data shown represent mean values of at least five independent determinations performed with the sera of distinct animals. The results are presented as means plus standard deviation (bars). HBV, hepatitis B virus.

of serum ALT (<100 U/l), which is in perfect accord with previous reports (16, 30). In contrast, serum ALT levels of Alb-1HBV SAP-IFNγ double-transgenic mice reached levels of about 300 U/l and were significantly (*T*-test, $P<0,05$) increased as compared with those of both single-transgenic mutants.

The significant elevation of serum ALT as found in double-transgenic Alb-1HBV SAP-IFNγ mice was in accordance with the previous detection (see Fig. 2B) of intensive mononuclear infiltrates in such livers. To further investigate IFNγ-mediated exacerbation of Alb-1HBV hepatitis, we quantitated the mononuclear infiltrates in livers of Alb-1HBV × SAP-IFNγ offspring mice by morphometric tools as described in Materials and method. We found that the mononuclear infiltrates of Alb1-1HBV SAP-IFNγ double-transgenic livers (mean of three animals: 9.5%, standard deviation: 6.6%) were significantly more extensive ($P<0.05$, *T*-test) as compared with Alb1-1HBV single-transgenic controls (mean of four animals: 0.6%, standard deviation: 1.0%). The inflammatory infiltrates of SAP-IFNγ single-transgenic livers were adequate compared

with those of Alb1-1HBV single-transgenic mice, and no mononuclear infiltrations could be detected in nontransgenic livers (not shown).

IFNγ coexpression increases hepatocellular apoptosis of Alb-1HBV mice

During the histological analyses as described in the last paragraph, we detected abundant numbers of Councilman bodies (Fig. 2B, asterisks) in the liver parenchyma of Alb1-1HBV SAP-IFNγ double-transgenic livers, whereas virtually no such eosinophilic structures could be observed in the Alb1-1HBV or SAP-IFNγ single-transgenic controls. As Councilman bodies are characteristic histological indicators of hepatocellular apoptosis, their increased appearance in double-transgenic livers suggested that the proinflammatory cytokine IFNγ had the potential to induce high-level hepatocellular apoptosis in Alb1-HBV transgenic mice. To test for this hypothesis, we determined α-PARP cleavage previously shown to represent a good marker of hepatocellular apoptosis (37) in the livers of double-transgenic, single-transgenic, and nontransgenic mice. As depicted in Fig. 4, no α-PARP cleavage was detectable in nontransgenic and in Alb-1HBV and SAP-IFNγ single-transgenic livers. In contrast, the PARP protein was completely cleaved in Alb-1HBV SAP-IFNγ double-transgenic livers.

In the following, we compared the hepatocellular proliferation rate of Alb-1HBV single-transgenic and Alb-1HBV SAP-IFNγ double-transgenic mice

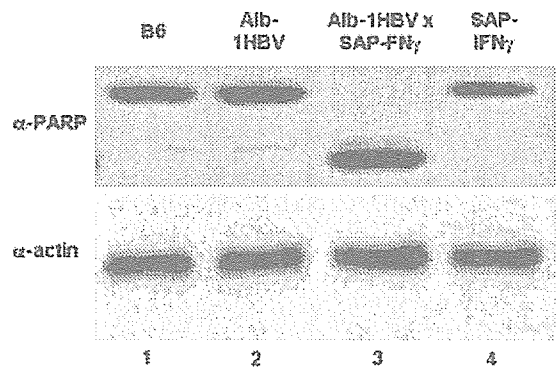

Fig. 4. Interferon γ (IFNγ) coexpression induces hepatocellular apoptosis in Alb-1HBV transgenic mice. Hepatic protein prepared from 2-month-old non-transgenic B6 (lane 1), Alb-1HBV single-transgenic (lane 2), Alb-1HBV SAP-IFNγ double-transgenic (lane 3), and SAP-IFNγ single-transgenic (lane 4) mice was separated by SDS-PAGE, blotted onto membranes, and stained with poly(ADP-ribose) polymerase (α-PARP) and actin-specific antisera. Note the complete α-PARP cleavage as detected in Alb-1HBV SAP-IFNγ double-transgenic livers (lane 3) indicative of massive hepatic apoptosis. No α-PARP cleavage could be found in Alb-1HBV (lane 2) and SAP-IFNγ (lane 4) single-transgenic livers as well as in non-transgenic controls (lane 1). HBV, hepatitis B virus.

by analyzing PCNA expression by immunohistochemistry and Western blotting. In these experiments, the Alb-1HBV SAP-IFNγ double-transgenic hepatocytes exhibited a slightly increased hepatocellular PCNA expression as compared with Alb-1HBV single-transgenic controls (data not shown).

Discussion

New drug delivery approaches (28, 29) may be suited to overcome the toxicological problems hitherto restricting the use of IFNγ for the therapy of chronic viral hepatitis. So far, the investigation of possible antiviral IFNγ effects in laboratory animal models has provided contradictory results. Whereas positive IFNγ effects could be observed in one study (28), the reports of other groups were less encouraging (38, 39), clearly indicating the need for further experimental research in this field. In the present study, we investigated the influence of transgenic IFNγ coexpression on the hepatic phenotype of LHBs-accumulating transgenic mice.

As LHBs retention sensitizes hepatocytes to IFNγ-mediated cytotoxic effects (35, 36), it could not be excluded that IFNγ coexpression might lead to perinatal death of Alb-1HBV transgenic mice. However, the double-transgenics were viable and showed a normal development up to an age of about 6 months. At higher age levels, Alb-1HBV SAP-IFNγ double-transgenic as well as SAP-IFNγ single-transgenic mice exhibited a significantly increased mortality, which resulted from cardiomyopathy induced by constitutive IFNγ serum expression (manuscript in preparation), and that is in complete accordance with the previous characterization of the lifespan of SAP-IFNγ transgenics (30).

IFNγ expression significantly reduced – but not completely suppressed – HBV surface gene expression. This antiviral IFNγ action may be mediated by the modulation of the RNA-binding activity of the La protein (40–42). The La protein binds to a predicted stem-loop structure located in the 5′ region of the HBV post-transcriptional regulatory element, which is harbored by all HBV surface transcripts of Alb1-HBV transgenic mice and that is thought to mediate the nuclear export of HBV RNA (43). The antiviral IFNγ effect observed had the potential to dramatically reduce hepatocellular LHBs storage disease, leading to inhibition of ground glass hepatocyte appearance of Alb1-HBV transgenic mice. Given the strong similarities between the Alb1-HBV mouse model and chronic hepatitis B, it can be assumed that high-level IFNγ expression in livers of HBV

carriers would also lead to significant impairment of hepadnaviral gene expression and to loss of storage disease and ground glass hepatocyte appearance. In this context, it should be mentioned that one hypothesis to explain hepatocellular LHBs overexpression during chronic hepatitis B implies integration of HBV DNA sequences into the host's genome, potentially bringing the LHBs reading frame under transcriptional control of strong host cell gene promoters (10). Alb1-HBV transgenic mice do precisely mimic such a scenario.

Very importantly, the positive antiviral IFNγ effects as observed in our murine model were associated with a significant exacerbation of liver inflammation. The inflammatory liver reactions of Alb-1HBV SAP-IFNγ double-transgenic mice showed a higher intensity than those of the single-transgenic counterparts, suggesting a synergistic proinflammatory action of IFNγ and HBV surface protein expression. This observation is in line with previous reports showing an increased susceptibility of LHBs expressing hepatocytes to cytotoxic IFNγ and/or TNFα actions (35, 36). In this context, it should be mentioned that a similar adverse effect of proinflammatory cytokines could recently be found in a woodchuck model of therapeutic vaccination aimed to shift the T-helper status of hepadnaviral immune responses from a Th2 to a Th1 type one. In this study, immunized animals developed massive hepatitis, which was found to be associated with liver-specific synthesis of IFNγ and TNFα (44). A further unwanted adverse reaction of IFNγ coexpression in Alb1-HBV transgenic livers was a significant increase of hepatocellular apoptosis. ALB1-HBV SAP-IFNγ double-transgenic livers show abundant infiltrates by IFNγ- activated macrophages and significantly elevated levels of TNFα transcription (data not shown). As TNFα biosynthesis is an important function of activated macrophages, it can be assumed that most parts of TNFα as expressed in ALB1-HBV SAP-IFNγ double-transgenic livers originate from macrophage biosynthesis. We speculate that the extraordinarily high TNFα levels as detected in ALB1-HBV SAP-IFNγ double-transgenic livers are responsible for the significantly increased apoptosis rate.

Summarizing, Alb-1HBV SAP-IFNγ double-transgenic mice provide an excellent model for investigating the suitability of liver-specific IFNγ gene therapy in patients with chronic hepatitis B. Our model on the one hand suggests that IFNγ expression in livers of patients with chronic hepatitis B would have the potential to reduce LHBs accumulation significantly and thus to inhibit ground glass hepatocyte appearance. However, on the other hand, our data propose that therapeutic liver-specific expression of IFNγ during chronic hepatitis B might be associated with exacerbation of hepatic necroinflammation and an increase of hepatic apoptosis. Both of these adverse IFNγ effects may accelerate cancer development during chronic hepatitis B (45–48). Therefore, particular measures of precautions are indispensable for testing approaches of liver-specific IFNγ expression in patients with chronic hepatitis B.

Acknowledgements

This work was supported by the Deutsche Forschungsgemeinschaft (Re 1030/2-2) and by grant 8312-38 62 61/527 of the 'Stiftung Rheinland-Pfalz für Innovation'. The excellent technical assistance of S. Maurer with the histological studies is gratefully acknowledged. We thank R. Schirmbeck (University of Ulm, Germany) for providing the polyclonal rabbit antibody recognizing all HBV surface proteins and for transferring Alb-1HBV breeders to the University of Mainz.

References

1. Chisari F V, Ferrari C. Hepatitis B virus immunopathogenesis. Annu Rev Immunol 1995; 13: 29–60.
2. Beasley R P. Hepatitis B virus. The major etiology of hepatocellular carcinoma. Cancer 1988; 61: 1942–56.
3. Shikata T. Australia antigen in liver tissue – an immunofluorescent and immunoelectron microscopic study. Jpn J Exp Med 1973; 43: 231–45.
4. Hadziyannis S, Gerber M A, Vissoulis C, Popper H. Cytoplasmic hepatitis B antigen in 'ground-glass' hepatocytes of carriers. Arch Pathol 1973; 96: 327–30.
5. Popper H. Clinical pathologic correlation in viral hepatitis. The effect of the virus on the liver. Am J Pathol 1975; 81: 609–28.
6. Popper H. The ground glass hepatocyte as a diagnostic hint. Hum Pathol 1975; 6: 517–20.
7. Gudat F, Bianchi L, Sonnabend W, Thiel G, Aenishaenslin W, Stalder G A. Pattern of core and surface expression in liver tissue reflects state of specific immune response in hepatitis B. Lab Invest 1975; 32: 1–9.
8. Bianchi L. Liver biopsy interpretation in hepatitis. Part I. Presentation of critical morphologic features used in diagnosis (glossary). Pathol Res Pract 1983; 178: 2–19.
9. Wang H C, Wu H C, Chen C F, Fausto N, Lei H Y, Su I J. Different types of ground glass hepatocytes in chronic hepatitis B virus infection contain specific pre-S mutants that may induce endoplasmic reticulum stress. Am J Pathol 2003; 163: 2441–9.
10. Dienes H P, Gerlich W H, Worsdorfer M, et al. Hepatic expression patterns of the large and middle hepatitis B virus surface proteins in viremic and nonviremic chronic hepatitis B. Gastroenterology 1990; 98: 1017–23.
11. Xu Z, Jensen G, Yen T S. Activation of hepatitis B virus S promoter by the viral large surface protein via induction of stress in the endoplasmic reticulum. J Virol 1997; 71: 7387–92.
12. Xu Z, Yen T S. Intracellular retention of surface protein by a hepatitis B virus mutant that releases virion particles. J Virol 1996; 70: 133–40.

13. Chisari F V, Pinkert C A, Milich D R, et al. A transgenic mouse model of the chronic hepatitis B surface antigen carrier state. Science 1985; 230: 1157–60.
14. Chisari F V, Filippi P, McLachlan A, et al. Expression of hepatitis B virus large envelope polypeptide inhibits hepatitis B surface antigen secretion in transgenic mice. J Virol 1986; 60: 880–7.
15. Chisari F V, Filippi P, Buras J, et al. Structural and pathological effects of synthesis of hepatitis B virus large envelope polypeptide in transgenic mice. Proc Natl Acad Sci USA 1987; 84: 6909–13.
16. Chisari F V, Klopchin K, Moriyama T, et al. Molecular pathogenesis of hepatocellular carcinoma in hepatitis B virus transgenic mice. Cell 1989; 59: 1145–56.
17. Dunsford H A, Sell S, Chisari F V. Hepatocarcinogenesis due to chronic liver cell injury in hepatitis B virus transgenic mice. Cancer Res 1990; 50: 3400–7.
18. Pasquinelli C, Bhavani K, Chisari F V. Multiple oncogenes and tumor suppressor genes are structurally and functionally intact during hepatocarcinogenesis in hepatitis B virus transgenic mice. Cancer Res 1992; 52: 2823–9.
19. Hagen M, Huang S, Curnutte J, et al. Extensive oxidative DNA damage in hepatocytes of transgenic mice with chronic active hepatitis destined to develop hepatocellular carcinoma. Proc Natl Acad Sci USA 1994; 91: 12808–12.
20. Huang N, Chisari F V. Strong, sustained hepatocellular proliferation precedes hepatocarcinogenesis in hepatitis B surface antigen transgenic mice. Hepatology 1995; 21: 620–6.
21. Uprichard S L, Wieland S F, Althage A, Chisari F V. Transcriptional and posttranscriptional control of hepatitis B virus gene expression. Proc Natl Acad Sci USA 2003; 100: 1310–5.
22. Robek M D, Boyd B S, Wieland S F, Chisari F V. Signal transduction pathways that inhibit hepatitis B virus replication. Proc Natl Acad Sci USA 2004; 101: 1743–7.
23. Guidotti L G Chisari F V. Cytokine-induced viral purging – role in viral pathogenesis. Curr Opin Microbiol 1999; 2: 388–91.
24. Guidotti L G, Ando K, Hobbs M V, et al. Cytotoxic T lymphocytes inhibit hepatitis B virus gene expression by a noncytolytic mechanism in transgenic mice. Proc Natl Acad Sci USA 1994; 91: 3764–8.
25. Guidotti T, Ishikawa M, Hobbs V, Matzke B, Schreiber R, Chisari F V. Intracellular inactivation of the hepatitis B virus by cytotoxic T lymphocytes. Immunity 1996; 4: 25–36.
26. Cavanaugh V J, Guidotti L G, Chisari F V. Interleukin-12 inhibits hepatitis B virus replication in transgenic mice. J Virol 1997; 71: 3236–43.
27. Kimura K, Kakimi K, Wieland S, Guidotti L G, Chisari F V. Interleukin-18 inhibits hepatitis B virus replication in the livers of transgenic mice. J Virol 2002; 76: 10702–7.
28. Dumortier J, Schonig K, Oberwinkler H, et al. Liver-specific expression of interferon gamma following adenoviral gene transfer controls hepatitis B virus replication in mice. Gene Ther 2005; 1: 1–10.
29. Kountouras J, Boura P, Kouklakis G. Locoregional immunochemotherapy in hepatocellular carcinoma. Hepatogastroenterology 2002; 49: 1109–12.
30. Toyonaga T, Hino O, Sugai S, et al. Chronic active hepatitis in transgenic mice expressing interferon-gamma in the liver. Proc Natl Acad Sci USA 1994; 91: 614–8.
31. Reifenberg K, Lohler J, Pudollek H P, et al. Long-term expression of the hepatitis B virus core-e- and X-proteins does not cause pathologic changes in transgenic mice. J Hepatol 1997; 26: 119–30.
32. Reifenberg K, Wilts H, Lohler J, et al. The hepatitis B virus X protein transactivates viral core gene expression *in vivo*. J Virol 1999; 73: 10399–405.
33. Pietsch K, Ehlers S, Jacobs E. Cytokine gene expression in the lungs of BALB/c mice during primary and secondary intranasal infection with Mycoplasma pneumoniae. Microbiology 1994; 140: 2043–8.
34. Breitfeld O, Kuhlcke K, Lother H, et al. Detection and spatial distribution of IL-2 receptors on mouse T-lymphocytes by immunogold-labeled ligands. J Histochem Cytochem 1996; 44: 605–13.
35. Gilles P N, Guerrette D L, Ulevitch R J, Schreiber R D, Chisari F V. HBsAg retention sensitizes the hepatocyte to injury by physiological concentrations of interferon-gamma. Hepatology 1992; 16: 655–63.
36. Ando K, Moriyama T, Guidotti L G, et al. Mechanisms of class I restricted immunopathology. A transgenic mouse model of fulminant hepatitis. J Exp Med 1993; 178: 1541–54.
37. Wesierska-Gadek J, Gueorguieva M, Wojciechowski J, Tudzarova-Trajkovska S. In vivo activated caspase-3 cleaves PARP-1 in rat liver after administration of the hepatocarcinogen N-nitrosomorpholine (NNM) generating the 85 kDa fragment. J Cell Biochem 2004; 93: 774–87.
38. Fiedler M, Rodicker F, Salucci V, et al. Helper-dependent adenoviral vector-mediated delivery of woodchuck-specific genes for alpha interferon (IFN-alpha) and IFN-gamma: IFN-alpha but not IFN-gamma reduces woodchuck hepatitis virus replication in chronic infection *in vivo*. J Virol 2004; 78: 10111–21.
39. Shin E C, Protzer U, Untergasser A, et al. Liver-directed gamma interferon gene delivery in chronic hepatitis C. J Virol 2005; 79: 13412–20.
40. Heise T, Guidotti L G, Cavanaugh V J, Chisari F V. Hepatitis B virus RNA-binding proteins associated with cytokine-induced clearance of viral RNA from the liver of transgenic mice. J Virol 1999; 73: 474–81.
41. Heise T, Guidotti L G, Chisari F V. La autoantigen specifically recognizes a predicted stem-loop in hepatitis B virus RNA. J Virol 1999; 73: 5767–76.
42. Heise T, Guidotti L G, Chisari F V. Characterization of nuclear RNases that cleave hepatitis B virus RNA near the La protein binding site. J Virol 2001; 75: 6874–83.
43. Huang J, Liang T J. A novel hepatitis B virus (HBV) genetic element with Rev response element-like properties that is essential for expression of HBV gene products. Mol Cell Biol 1993; 13: 7476–86.
44. Hervas-Stubbs S, Lasarte J J, Sarobe P, Et al. Therapeutic vaccination of woodchucks against chronic woodchuck hepatitis virus infection. J Hepatol 1997; 27: 726–37.
45. Nakamoto Y, Guidotti L G, Kuhlen C V, Fowler P, Chisari F V. Immune pathogenesis of hepatocellular carcinoma. J Exp Med 1998; 188: 341–50.
46. Takeda K, Smyth M J, Cretney E, et al. Critical role for tumor necrosis factor-related apoptosis-inducing ligand in immune surveillance against tumor development. J Exp Med 2002; 195: 161–9.
47. Kountouras J, Zavos C, Chatzopoulos D. Apoptosis in hepatocellular carcinoma. Hepatogastroenterology 2003; 50: 242–9.
48. Schuchmann M, Galle P R. Sensitizing to apoptosis – sharpening the medical sword. J Hepatol 2004; 40: 335–6.

Abnormal migration and distribution of neural crest cells in Pax6 heterozygous mutant eye, a model for human eye diseases

Sachiko Kanakubo[1,2], Tadashi Nomura[1], Ken-ichi Yamamura[3], Jun-ichi Miyazaki[4], Makoto Tamai[2] and Noriko Osumi[1,5,*]

[1]*Division of Developmental Neuroscience, Center for Translational and Advanced Animal Research, Tohoku University Graduate School of Medicine, 2-1, Seiryo-machi, Aoba-ku, Sendai, 980-8575, Japan*
[2]*Department of Ophthalmology, Tohoku University Graduate School of Medicine, 1-1, Seiryo-machi, Aoba-ku, Sendai, 980-8575, Japan*
[3]*Division of Developmental Genetics, Institute of Molecular Embryology and Genetics, Kumamoto University, 4-24-1, Kuhonji, Kumamoto, 862-0976, Japan*
[4]*Division of Stem Cell Regulation Research, Osaka University Graduate School of Medicine, 2-2 Yamadaoka, Suita, Osaka 565-0871, Japan*
[5]*CREST Japan Science and Technology Agency, 4-1-8, Honcho, Kawaguchi, 332-0012 Japan*

PAX6/Pax6 **gene encodes a transcription factor that is crucially required for eye development. Pax6 heterozygous mutant mouse (*Pax6*$^{Sey/+}$) shows various ocular defects, especially in the anterior segment. It has been well known that the induction of the lens and development of the cornea and retina are dependent on *PAX6/Pax6* in a cell-autonomous fashion, although the influence of *PAX6/Pax6* on the other tissues derived from the ocular mesenchyme is largely unknown. Using transgenic mouse lines in which neural crest cells are genetically marked by LacZ or EGFP, we revealed the extensive contribution of neural crest derived cells (NCDCs) to the ocular tissues. Furthermore, various eye defects in *Pax6*$^{Sey/+}$ mouse were accompanied by abnormal distribution of NCDCs from early developmental stages to the adult. In *Pax6*$^{Sey/+}$ mouse mice, neural crest cells abnormally migrated into the developing eye in a cell nonautonomous manner at early embryonic stages. These results indicate that normal distribution and integration of NCDCs in ocular tissues depend on a proper dosage of Pax6, and that *Pax6*$^{Sey/+}$ eye anomalies are caused by cell autonomous and nonautonomous defects due to *Pax6* haploinsufficiency.**

Introduction

In vertebrates, the eye originates from three different tissues, the head ectoderm, the neuroepithelium and the mesenchyme. The surface ectoderm later forms the lens and corneal epithelium, while the neuroepithelium gives rise to the neural retina and the retinal pigment epithelium. All other tissues in the eye are derived from the ocular mesenchyme. The ocular mesenchyme includes cells that originate from both the mesoderm and the neural crest, as demonstrated in the quail-chick chimera system (Le Douarin & Kalcheim 1999). For example, the neural crest contributes to the formation of the corneal endothelium and stromal cells (Hay *et al.* 1979; Johnston *et al.* 1979; Meier 1982; Nakamura 1982). More recently, extensive research in avian embryos (Creuzet *et al.* 2005) has shown that cranial neural crest cells (NCCs) give rise not only to the cornea but also to other intra- and extra-ocular structures such as the iris, ciliary body, choroid, sclera and part of the extra-ocular muscles.

In mice, vital dye analyses have indicated that NCCs from the midbrain and forebrain normally migrate to the craniofacial region including the prospective ocular mesenchyme (Serbedzija *et al.* 1992; Osumi-Yamashita *et al.* 1994; Trainor & Tam 1995). The ocular mesenchyme is thought to play an important role in the morphogenesis of the anterior eye segment in mammals (Cvekl & Tamm 2004). However, these studies have not revealed the precise contribution of the neural crest to eye development due to the lack of suitable markers for murine NCCs and the methodological limitation of tracing labeled cells through the later stages. Recently, genetic marking using Cre-recombinase has been applied to the long-term tracing of NCCs in *Wnt1-Cre, protein zero (P0)-Cre* and *HTPA-Cre* mice (Danielian *et al.* 1998;

Communicated by: Masayuki M. Yamamoto
**Correspondence*: E-mail: osumi@mail.tains.tohoku.ac.jp

DOI: 10.1111/j.1365-2443.2006.00992.x

Yamauchi *et al.* 1999; Jiang *et al.* 2000; Pietri *et al.* 2003). Specifically, Matt *et al.* (2005) utilized *Wnt1-Cre* mice, reporting involvement of NCLDCs in the ocular mesenchyme. This suggests that NCCs could be controlling their migration and distribution during ocular morphogenesis by various factors.

The *PAX6/Pax6* gene encodes a transcription factor and was initially identified as the responsible gene for human aniridia disease and mouse *Small eye* mutant (*Pax6*$^{Sey/+}$) (Hill *et al.* 1991; Ton *et al.* 1991). *Pax6* is expressed in developing ocular tissues including the lens, corneal epithelium, iris, ciliary body, and all layers of the retina (Grindley *et al.* 1995). Mutations within human *PAX6* gene cause a spectrum of eye phenotypes in the whole eyeball, including cataract, iris hypoplasia, corneal opacification and foveal dysplasia (Glaser *et al.* 1994; Hanson & van Heyningen 1995; Mirzayans *et al.* 1995; Azuma *et al.* 2003). In mouse, *Pax6*$^{Sey/+}$ has a base pair substitution creating a premature stop codon in the linker region (Hill *et al.* 1991), and *Pax6*$^{Sey/+}$ mice show ocular anomalies corresponding to human eye diseases (Hogan *et al.* 1988; Baulmann *et al.* 2002; Ramaesh *et al.* 2003). We have also identified similar eye defects in *Small eye* rat strains that have spontaneous nonsense mutations in the *Pax6* gene (Matsuo *et al.* 1993; Osumi *et al.* 1997).

Homozygous *Pax6* mutant mice/rats are eyeless due to failure to respond to induction signals from the optic vesicle (Fujiwara *et al.* 1994). Interestingly, these *Pax6* mutants show not only anophthalmia but also various craniofacial defects including the absence of nasal structures and duplication of the upper teeth (Hogan *et al.* 1988; Quinn *et al.* 1997). Our previous studies demonstrated that the craniofacial defects were due to impaired migration of midbrain crest cells (Matsuo *et al.* 1993; Osumi-Yamashita *et al.* 1997). However, the mechanism for ocular defects in *Pax6*$^{Sey/+}$ has not been studied with reference to NCCs.

Here we report the results of comprehensive phenotype analyses of *Pax6*$^{Sey/+}$ eyes with reference to human eye diseases. To analyze the precise contribution of NCCs to eye development, we used *P0-Cre* transgenic mouse in which Cre recombination specifically occurred in migrating NCCs when it crosses with *CAG-CAT-Z* or *CAG-CAT-EGFP* line (Yamauchi *et al.* 1999; Kawamoto *et al.* 2000). By genetically marking neural crest-derived cells (NCLDCs) in transgenic mice, we were able to identify the contribution of these cells to the development of intra- and peri-ocular tissues in both wild-type and *Pax6*$^{Sey/+}$. We also showed that impaired migration of NCLDCs nonautonomously leads to eye anomalies in *Pax6*$^{Sey/+}$ mutant mice, suggesting that defects in the anterior and posterior segments of the eye are due to abnormal distribution and integration of NCLDCs.

Results

Eye defects in the adult Pax6$^{Sey/+}$ mouse

In human, haploinsufficiency in *PAX6* gene causes various ocular anomalies (Prosser & van Heyningen 1998; Vincent *et al.* 2003). The *Small eye* mutant mouse with a mutation in the orthologous *Pax6* gene is thus considered a suitable animal model for aniridia based on the phenotypic similarities (Hogan *et al.* 1988; Baulmann *et al.* 2002; Ramaesh *et al.* 2003). However, previous analyses have not shown the comparison of ocular anomalies, such as aniridia and Peters anomaly (Kenyon 1975), between human and *Small eye* mutant mouse. *Pax6*$^{Sey/+}$ eyes showed various phenotypes not only in the size of the eye and structures of the lens and retina but also in other tissues of the ocular anterior segments and vitreous body (Table 1, Fig. 1A). The phenotype shows significant variation, some of it stochastic, with differences between the right and left eyes in the same mouse (see no. 2 vs. no. 10 and no. 20 vs. no. 28, Table 1). Corneal opacity was a typical phenotype observed in all *Pax6*$^{Sey/+}$ eyes. Some of the smaller eyes showed sclerocornea, scleralization of the anterior surface of the eye globe, associated with corneal flattening and opacity (4/28 cases) (Fig. 1A; *Pax6*$^{Sey/+}$ no. 4). Severe opacity was associated with peripheral vascularization of the cornea (Fig. 1A; *Pax6*$^{Sey/+}$ no. 6). Complete lack of the iris was observed only in one (Table 1, no. 1) of 28 cases, but partial defects and reduction of the iris were frequently seen in the phenotype corresponding to aniridia. Keratolenticular strands, which are tissues bridging between the cornea and lens (arrow in Fig. 1A; *Pax6*$^{Sey/+}$ no. 19), were also seen, leading to reduction of the anterior chamber. Irido-corneal synechia, i.e. adhesion of the iris to the cornea, was often detected (20/28 cases), and in severe cases, the anterior chamber and the angle were narrow or disappeared totally (Fig. 1A; *Pax6*$^{Sey/+}$ no. 4, *Pax6*$^{Sey/+}$ no. 6). Peters anomaly, which includes a central corneal opacity with underlying defects in the posterior stroma, Descemet membrane and corneal endothelium, and sometimes accompanied by cornea–lens adhesion (6/28 cases with asterisks in Table 1). In the posterior part of the eye, loss of a part of the eye tissues (coloboma) was noted in the chroid in association with a partial defect of the iris in 9/28 cases. Abnormal cell accumulation in the vitreous cavity was detected in 10/28 cases, and a vessel-like structure was noted in severe cases (arrowheads in Fig. 1A; *Pax6*$^{Sey/+}$ no. 4, *Pax6*$^{Sey/+}$ no. 6).

Table 1 A wide spectrum of ocular abnormalities in *Pax6*$^{Sey/+}$

Eye Sample	Axial length (mm)	Corneal opacity	Peripheral vascularization	Sclerocornea	Endothelium defect	Keratolenticular strands	Iris synechia	Coloboma	Cataract	Vitreous cell accumulation	Retinal dysplasia
No. 1	1.3	+	–	+	–	–	NI	–	NL	+	+
2	1.9	+	–	+	–	–	+ NA	–	NL	+	+
3	2.2	+	+	+	–	–	+ NA	+	+	+	+
4	2.4	+	+	+	–	–	+ NA	–	+	+	+
5*	2.9	+	+	–	+	+	+ NA	–	+	–	+
6	3.0	+	+	–	–	–	+ NA	–	+	+	+
7*	3.0	+	+	–	+	–	+ NA	+	+	+	–
8	3.0	+	+	–	–	–	+ NA	+	+	+	–
9	3.1	+	+	–	–	–	+	+	+	+	+
10	3.1	+	+	–	–	+	+	+	+	+	+
11*	3.1	+	+	–	+	+	+	–	+	–	–
12	3.1	+	+	–	–	+	+	–	+	–	+
13	3.2	+	+	–	–	–	+ NA	+	+	+	+
14	3.2	+	+	–	–	+	+	+	+	–	–
15	3.2	+	–	–	–	–	+	+	+	–	–
16	3.2	+	–	–	–	+	+	–	+	–	–
17*	3.3	+	–	–	+	–	+	+	+	–	–
18	3.3	+	–	–	–	+	+	–	+	–	–
19	3.3	+	–	–	–	+	–	–	+	–	–
20	3.3	+	–	–	–	+	+	–	+	–	–
21	3.3	+	–	–	–	–	–	–	+	–	–
22*	3.4	+	–	–	+	+	+	–	+	–	–
23	3.4	+	–	–	–	+	+	–	+	–	–
24	3.4	+	–	–	–	+	–	–	+	–	–
25	3.4	+	–	–	–	–	–	–	–	–	–
26*	3.4	+	+	–	+	–	–	–	–	–	–
27	3.5	+	–	–	–	–	–	–	–	–	–
28	3.5	+	+	–	–	–	–	–	–	–	–
Total		28/28	14/28	4/28	6/28	12/28	20/28	9/28	22/28	10/28	10/28
(%)		(100)	(50.0)	(14.3)	(21.4)	(42.8)	(71.4)	(32.1)	(78.6)	(35.7)	(35.7)

NI: No Iris; NA: No Angle; NL: No Lens.

*Peters anomaly: phenotype showing corneal endothelial defects with or without cornea-lens adhesion. Coloboma: defects of the ocular tissue; Sclerocornea: cornea presents scleral characteristics; Keratolenticular strands: tissues bridging between the cornea and lens; Irido-corneal synechia: adhesions of iris to the cornea.

The above-mentioned anomalies were never seen in wild-type eyes (n = 20; Fig. 1A; wild-type). Although the size of individual *Pax6*$^{Sey/+}$ eyes varied widely from less than half of the normal eye to nearly the same as the normal, the weight and the axial length of *Pax6*$^{Sey/+}$ eyes were significantly smaller than those of the wild-type (Fig. 1B,C). Notably, the severity of abnormalities correlated well with the eye size (Table 1, Fig. 1A). These results indicate that individual *Pax6*$^{Sey/+}$ eyes show a wide spectrum of phenotypes reflecting not only defects directly due to loss of Pax6 function but also because of altered behavior of the ocular mesenchyme that is originally negative for Pax6 expression (see below).

Identification of NCDCs in P0-Cre transgenic mouse

Some lines of transgenics, such as *Wnt1-Cre*, *P0-Cre*, and *HTPA-Cre* mice, are now available for genetically marking NCCs (Danielian *et al.* 1998; Yamauchi *et al.* 1999; Jiang *et al.* 2000; Pietri *et al.* 2003). In this study, it was favorable for us to use albino mice to avoid pigmentation in the retinal pigment epithelium and iris. Therefore, we used the *P0-Cre* transgenic line (Yamauchi *et al.* 1999) because the expression patterns of reporter genes were unchanged, unlike those in the *HTPA-Cre* line, even though *P0-Cre* transgenic mice were crossed with CD-1 mice (albino color) for 5–6 generations.

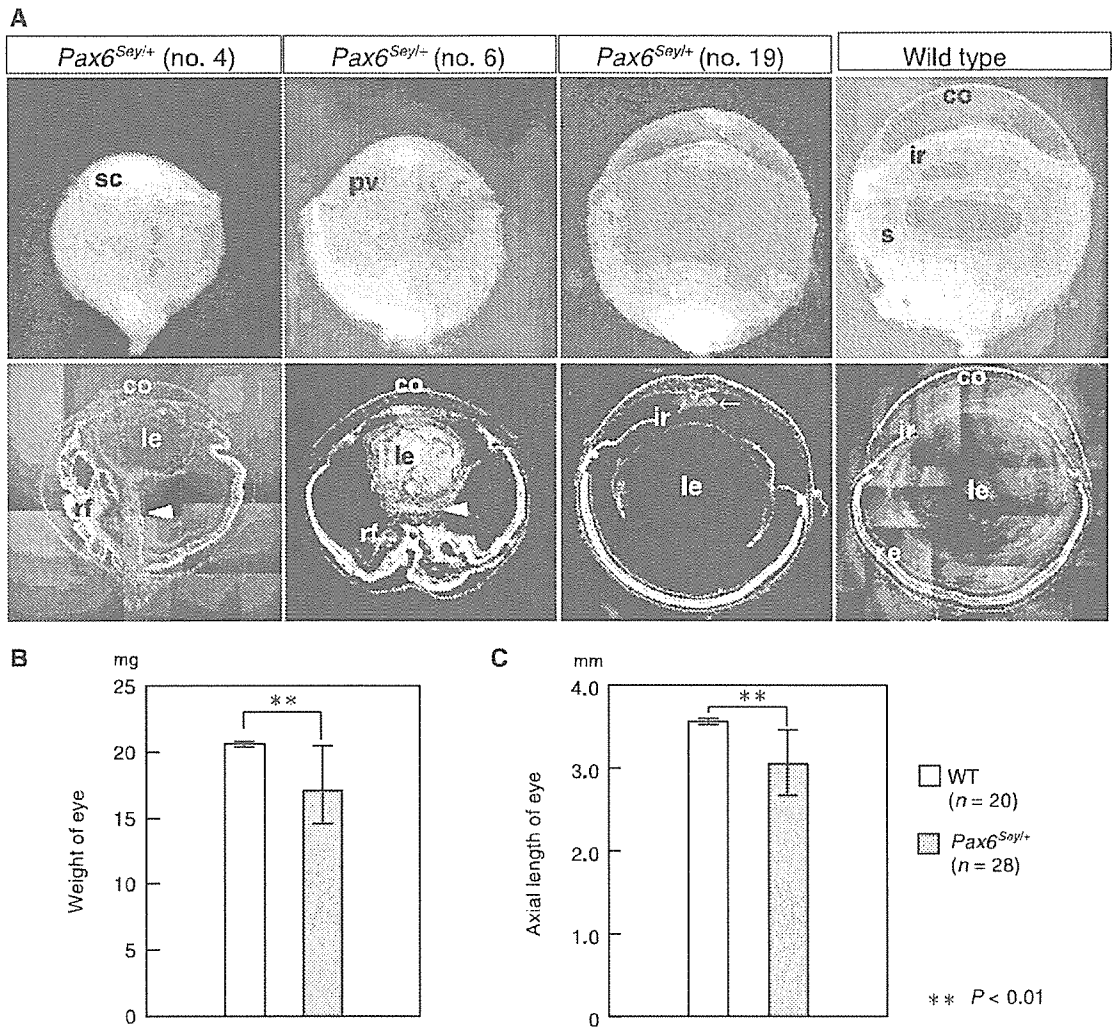

Figure 1 Various phenotypes in the adult *Pax6*$^{Sey/-}$ eyes. Eyes obtained from 6-week-old *Pax6*$^{Sey/-}$ mice on *P0-Cre*; *CAG-CAT-EGFP* double transgenic background were analyzed. (A) Structures of the wild-type and *Pax6*$^{Sey/-}$ eyes. Green arrows indicate keratolenticular strands that bridge between the lens and cornea (*Pax6*$^{Sey/-}$ no. 19). Green arrowheads indicate accumulation of cells in the vitreous (*Pax6*$^{Sey/-}$ no. 6, no. 4). co, cornea; ir, iris; a, anterior chamber angle; re, retina; le, lens; pv; peripheral vascularization of cornea; rf, retinal fold; s, sclerocornea. (B, C) Both the weight (B) and size (C) of *Pax6*$^{Sey/-}$ eyes (▨) are smaller than those of the wild-type (□). Data are mean ± SD of 20 eyes of the wild-type and of 28 eyes of *Pax6*$^{Sey/-}$.

Crossing *P0-Cre* line with *CAG-CAT-Z*Tg line led to lacZ expression by Cre-mediated recombination at stages after E9.0 in tissues considered as neural crest derivatives in the chick (Fig. 2A). To confirm directly the specificity of marking NCCs by this system, we crossed *P0-Cre* Tg line with *CAG-CAT-EGFP* Tg line (Kawamoto *et al.* 2000), and labeled migrating NCCs with DiI at E8.25. The embryos were cultured in a whole embryo culture system (Osumi-Yamashita *et al.* 1994) (Fig. 2B,C). DiI-labeled cells from the anterior hindbrain migrated ventrally to the first pharyngeal arch and to the trigeminal ganglion after 36 h in culture (corresponding to E9.5; Fig. 2D–F). GFP expression was clearly observed in the cytoplasm of cells labeled by DiI (Fig. 2G–J). The proportion of GFP-positive cells among DiI-labeled cells was 48.3 ± 3.9% (n = 3) in the area corresponding to the pathway of migration (arrowhead in Fig. 2F), and 95.7 ± 1.0% (n = 3) in the area corresponding to the migration terminal (arrow in Fig. 2F). These results suggest that *P0-Cre* activity is specific for migrating NCCs and NCDCs.

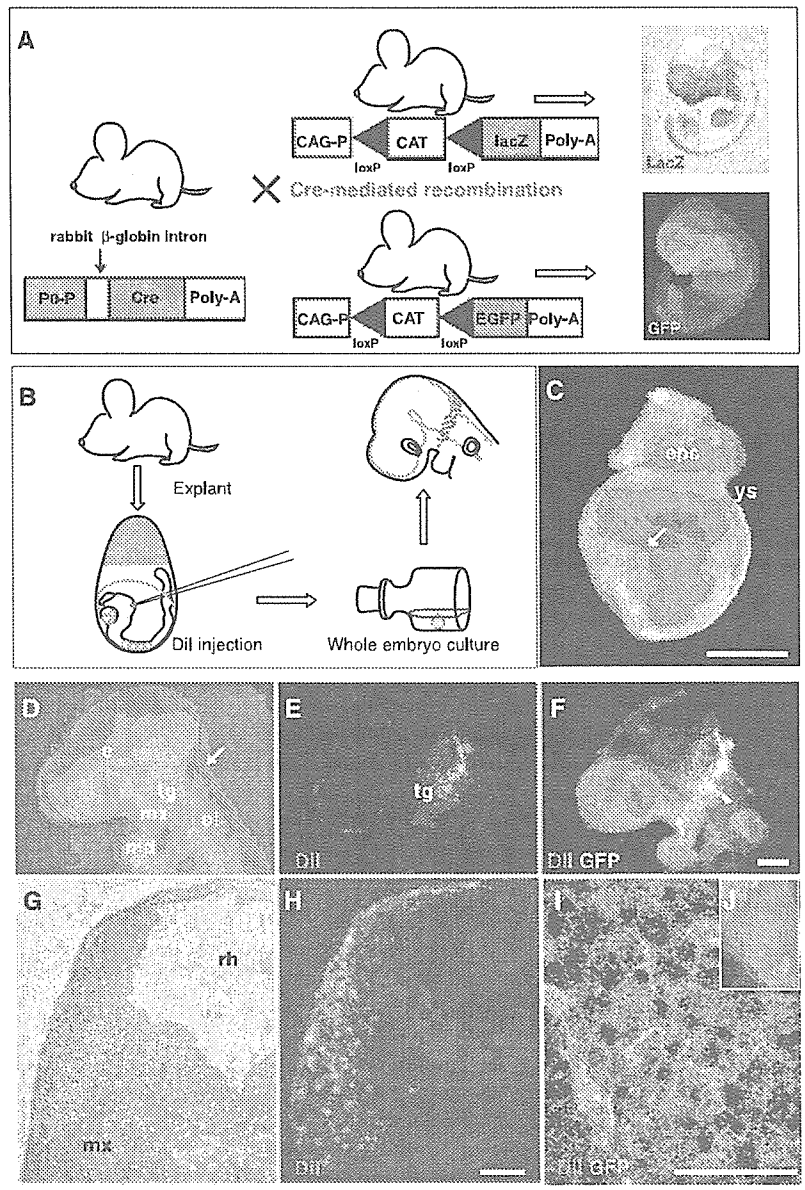

Figure 2 Strategy and specificity of genetic marking of NCDCs in mice. (A) By genetically marking neural crest-derived cells (NCDCs), *P0-Cre* Tg mice were crossed with *CAG-CAT-Z* Tg mice or *CAG-CAT-EGFP* Tg mice to obtain lacZ or GFP expression after Cre-mediated recombinase. (B, C) E8.25 (4-somite stage) embryos on *P0-Cre*; *CAG-CAT-EGFP* Tg background were labeled with DiI (arrow in C), and cultured for 36 h (up to 25–30 somite stage). epc, ectoplacental cone; ys, yolk sac. (D–F) DiI-labeled cells migrate ventrally to the first pharyngeal arch including maxillary (mx) and mandibular (md) prominences. e, eye primordium; tg, trigeminal ganglion; ot, otic vesicle. (G–J) Transverse sections show GFP expression in the cytoplasm of cells with DiI-positive membrane. rh, rhombencephalon. Scale bars (C) 500 μm; (F) 1 mm; (H, I) 50 μm.

Altered distribution of NCDCs from early embryonic stages in *Pax6*$^{Sey/+}$ mice

As described above, *Pax6*$^{Sey/+}$ adult eyes showed variable phenotypes in tissues derived from the ocular mesenchyme. We focused on the onset of ocular defects in *Pax6*$^{Sey/+}$ from the viewpoint of developmental association with NCCs. For this purpose, we analyzed the distribution of NCDCs by using *P0-Cre*; *lacZ* and *P0-Cre*; *EGFP* double Tg embryos in the wild-type and in *Pax6*$^{Sey/+}$ backgrounds.

During E9.5–E10.5, lacZ expression was observed in various craniofacial regions including the frontonasal mass, maxillary and mandibular prominences in both the wild-type and *Pax6*$^{Sey/+}$ embryos (Fig. 3A, B,D,E). A slight difference in lacZ expression patterns in the two genotypes became evident at E11.5. In *Pax6*$^{Sey/+}$ embryos, which often showed smaller lenses, lacZ expression was more intense at the temporal part adjacent to the eye primordium (black arrow in Fig. 3F), while reduction or loss of lacZ expression was observed in the lateral nasal prominence (white arrow in Fig. 3F compared with

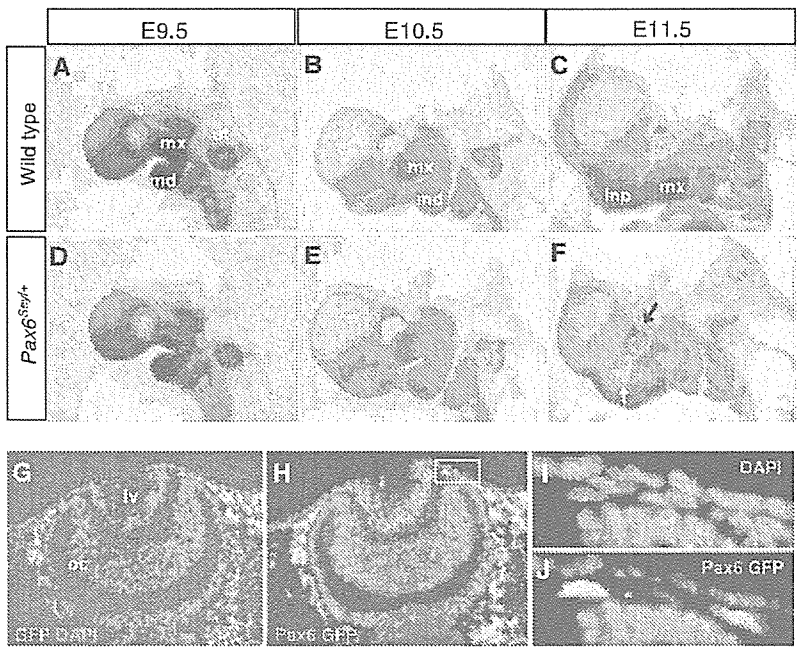

Figure 3 Altered distribution of NCDCs around the eye of *Pax6*$^{Sey/-}$ at E11.5. (A–F) lacZ and GFP expression indicate the distribution of NCDCs in the craniofacial region of the wild-type (A–C) and *Pax6*$^{Sey/-}$ (D–F) from E9.5 to E11.5. At E11.5, *Pax6*$^{Sey/-}$ embryo has a small lens with more intense lacZ expression in the temporal part adjacent to the eye (black arrow in F), while reduced lacZ expression is observed in the lateral nasal prominence (lnp, white arrow in F). e, eye primordium; mx, maxillary prominence; md, mandibular prominence; ot, otic vesicle. (G–J) Immunostaining with anti-Pax6 antibody demonstrates the expression of Pax6 (magenta) in the surface ectoderm, lens vesicle (lv) and optic cup (oc) (G, H), but not in GFP-labeled NCDCs (green) at E10.5. (I, J) High magnification images of the boxed area in H.

Fig. 3C). Immunohistochemical staining for Pax6 protein showed that the expression was observed in the surface ectoderm, lens vesicle and optic cup, but not in the GFP-labeled cells (Fig. 3G–J). These results indicate that NCDCs, which are marked with lacZ or GFP, are negative for Pax6 expression, populate in the neighboring areas of the eye primordium by E11.5. In addition, more NCDCs seem to accumulate in the temporal side of the eye primordium rather than in the nasal side in *Pax6*$^{Sey/+}$ embryos.

We investigated which population of the NCDCs contributes predominantly to the ocular structure. The periocular mesenchyme was labeled with DiI at either the temporal or nasal side of the eye primordium in wild-type embryos at E10.0 (Fig. 4A,D), and the labeled embryos were cultured for 36 h. DiI-labeled temporal-side cells were observed in the eye structure (Fig. 4B,C). Furthermore, these cells were seen beneath the surface ectoderm and the prospective vitreous in the section corresponding to the migration of midbrain NCCs (Fig. 4G). In contrast, the cells labeled at the nasal periocular mesenchyme migrated to the nasal prominence, and they were not observed in the eye (Fig. 4E,F). Therefore, it is likely that NCCs originating from the midbrain contribute to the eye tissues.

Next we examined histologically the development of the eye of wild-type and *Pax6*$^{Sey/+}$ embryos during E9.5–11.5. At E9.5 and E10.5, morphological difference was not observed in *Pax6*$^{Sey/+}$ eye primordium (data not shown). At E11.5, the lens vesicle was completely separated from the surface ectoderm in the wild-type, and most of the mesenchyme around the eye primordium expressed GFP (green cells in Fig. 5B). Notably, some GFP-labeled cells were identified in the space between the lens and optic cup (arrow in Fig. 5B). Compared with the wild-type, *Pax6*$^{Sey/+}$ eyes frequently showed smaller lens vesicle and optic cup and incomplete lens separation from the surface ectoderm (arrowhead in Fig. 5C). Moreover, a large number of GFP-labeled cells accumulated within the vitreous cavity (arrow in Fig. 5C). Thus we showed that morphological abnormalities of *Pax6*$^{Sey/+}$ eyes become apparent around E11.5 when separation of the lens is finished.

We further quantified accumulation of NCCs in the temporal and nasal sides of the eye primordium of the wild-type and *Pax6*$^{Sey/+}$ embryos at E11.5. Sections were made parallel to the plane of the migration pathway of the midbrain neural crest cells (line in Fig. 5A) and GFP-labeled cells were counted in the nasal and temporal areas (Fig. 5B,C). In the temporal area, the number of GFP-labeled cells of *Pax6*$^{Sey/+}$ embryos was significantly higher than that of the wild-type (Fig. 5D; $P = 0.0024$). On the other hand, there was no difference between the number of GFP-labeled cells in the nasal area of the wild-type and *Pax6*$^{Sey/+}$ ($P = 0.57$). We next investigated whether the accumulation of NCDCs around *Pax6*$^{Sey/+}$ eyes was due to increased cell proliferation. The percentage of BrdU-incorporated cells relative to GFP-labeled cells was similar in the two genotypes (wild-type: 28.3%; *Pax6*$^{Sey/+}$: 25.4% in Fig. 5E), suggesting that the cell accumulation

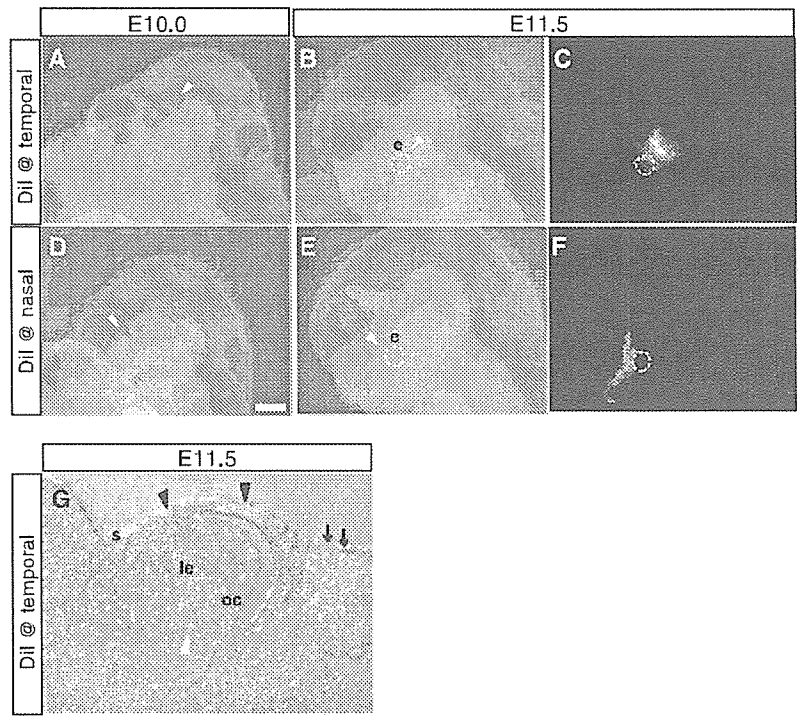

Figure 4 Mesenchymal cells at the temporal side of the eye primordium migrate and contribute to the vitreous structure. (A, B, D, E) NCCs are labeled by DiI at E10.0 (arrowhead in A and D) and the embryos are cultured for 36 h (B, E). (C) Mesenchymal cells labeled at the temporal side of the eye primordium are migrating into the eye (e) region. (F) Mesenchymal cells labeled at the nasal side of the eye primordium are migrating further toward the frontnasal area. White circles in (B, C, E, F) indicate the eye area. (G) Section (from the same sample shown in Figure 4C) is cut parallel to the plane along the migration pathway of the midbrain crest cells. DiI labeled cells are observed beneath the surface ectoderm (black arrowheads) in addition to the prospective vitreous cavity (white arrowhead). Arrows indicate the labeled area at E10.0. s, surface ectoderm; le, lens; oc, optic cup. Scale bar (D) 1 mm.

in *Pax6*$^{Sey/+}$ does not represent increased cell proliferation. These results suggest that the altered distribution of NCLDCs in the periocular region is due to the abnormal migration of midbrain crest cells in *Pax6*$^{Sey/+}$.

Abnormal distribution of NCDCs in *Pax6*$^{Sey/+}$ eyes at later stages

We further examined the contribution of NCLDCs at later stages of eye development. At E18.5, GFP-labeled cells were distributed in the cornea, choroid and sclera of the wild-type (Fig. 6A,B). In addition, a small number of GFP-labeled cells were found in the vitreous cavity, and some of these were recognized along with PECAM-positive vascular endothelial cells (data not shown). It is thus assumed that NCLDCs would contribute to the pericytes of the vitreous vessels, as shown in avian embryos (Etchevers *et al.* 2001; Korn *et al.* 2002). GFP-labeled cells accumulated in the angle between the cornea and the anterior edge of the optic cup, the latter of which subsequently forms the iris tissue (arrowheads in Fig. 6F). At this stage, Pax6 was expressed in the corneal epithelium, the lens epithelium, neural retina and retinal pigment epithelium (Fig. 6E,F). Notably, GFP-labeled NCLDCs never expressed Pax6, as well as in the early stages (Fig. 3H,J).

In contrast to the wild-type, *Pax6*$^{Sey/+}$ embryos exhibited various eye anomalies accompanied by different distribution of GFP-labeled cells both in the anterior and posterior eye segments. In a severe phenotype with a hypoplastic lens (Fig. 6C,D), abnormal accumulation of GFP-labeled cells was seen in the anterior chamber (arrowheads in Fig. 6H). Moreover, the most distal tip of the optic cup was irregularly folded, and the retinal pigment epithelium was obscure (Fig. 6D,G). Expression of Pax6 was reduced in the *Pax6*$^{Sey/+}$ eye (Fig. 6H), especially in the distal part of the retina compared with the wild-type (Fig. 6F). In the posterior eye segment, numerous GFP-positive cells were still observed within the vitreous cavity (Fig. 6C). Compared with wild-type, GFP-positive cells in the vitreous never formed a normal vascular structure (Fig. 6A). This cell accumulation in the vitreous cavity could be traced back to E11.5, and these NCLDCs never expressed Pax6 (data not shown). These results suggest that the abnormal distribution of NCLDCs in the early stage may result in the subsequent abnormal eye phenotypes in *Pax6*$^{Sey/+}$.

Identification of NCDCs in defective eye tissues of the adult *Pax6*$^{Sey/+}$ mice

We next examined the distribution of NCLDCs in adult eye tissues to determine the association of NCLDCs in the ocular anomalies found in *Pax6*$^{Sey/+}$mice. In the wild-type, GFP-labeled NCLDCs were distributed in the sclera, the

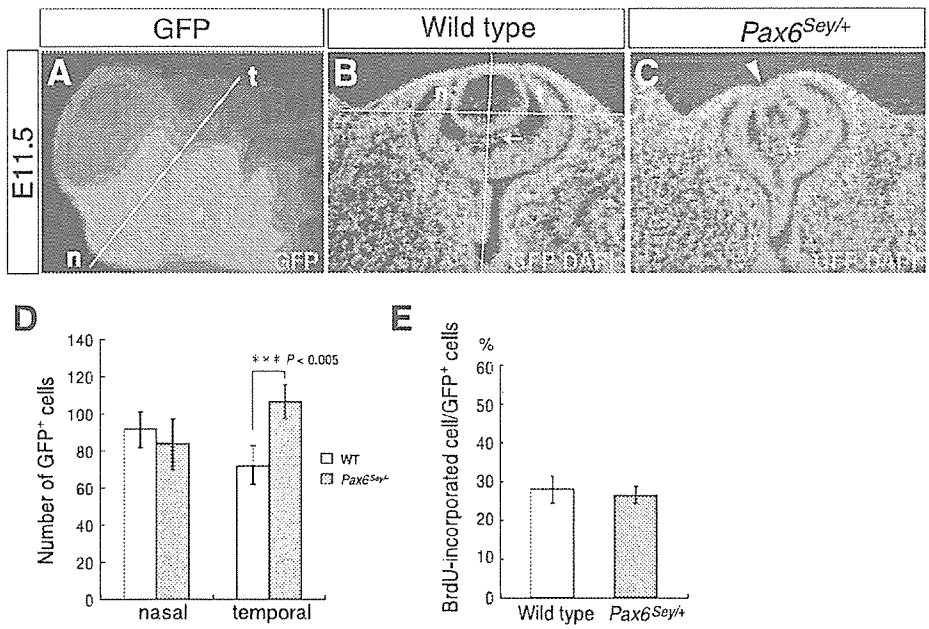

Figure 5 GFP-labeled NCDCs in temporal side of the eye are increasing in the *Pax6*$^{Sey/-}$ at E11.5. (A–C) To quantify the NCDCs around the eye primordium, sections are made parallel to the plane along the migration pathway of the midbrain crest cells (line in A) and GFP-labeled cells are counted in nasal (n) and temporal areas (t) both wild-type and *Pax6*$^{Sey/-}$ embryos, respectively. (B) In the wild-type *P0-Cre*; *CAG-CAT-EGFP* embryo, separation of the lens is complete by E11.5, and most of the mesenchymal cells around the eye and in the vitreous cavity (arrow) are labeled with GFP. (C) The *Pax6*$^{Sey/-}$ eye shows smaller lens vesicles and incomplete lens separation from the surface ectoderm (arrowhead) and cell accumulation in the vitreous cavity (arrow). (D) The number of GFP-labeled cells of *Pax6*$^{Sey/-}$ embryos in the temporal side was significantly higher than that of wild-type (n = 10). (E) The rate of cell proliferation is evaluated by counting double-immunostaining with antibodies for BrdU and GFP. The cell proliferation around the eyes is similar in the wild-type and in *Pax6*$^{Sey/-}$ eyes.

iris stroma and the ciliary body (Fig. 7A,B,I). These cells were also seen in the chamber angle tissue including the trabecular meshwork and Schlemm's canal, the latter of which is known to play important roles in humor outflow (Fig. 7J). Furthermore, NCDCs were also observed in the corneal stroma and endothelium but not in the corneal epithelium (Fig. 7K). These results are in agreement with the findings of a recent study in the chick (Creuzet *et al.* 2005).

In *Pax6*$^{Sey/+}$ eyes, the defects shown in Table 1 correlated with abnormal distribution of NCDCs. For example, coloboma was observed as an area containing a small number of GFP-labeled cells (Fig. 7C; arrows in Fig. 7D). The defects of the anterior eye segment were frequently associated with aberrant distribution of NCDCs (Fig. 7E–H,L–N). For instance, keratolenticular strands were detected with corneal opacity in the central cornea, where abundant GFP-labeled cells were noted (arrow in Fig. 7G,H). Although the cornea in *Pax6*$^{Sey/+}$ developed into three layers like in the wild-type eyes, the structure of each layer was abnormal; the corneal stroma was thicker in the central region with an irregular lamellar alignment, and many GFP-positive cells were present in the thickened corneal endothelium (Fig. 7H,N). Furthermore, the hypoplastic iris stroma and ciliary body in *Pax6*$^{Sey/+}$ eyes contained fewer GFP-labeled cells (Fig. 7L,M) than in the wild-type (Fig. 7I). In contrast, the anterior iris stroma adherent to the cornea showed intense GFP expression (Fig. 7L). In severe cases of *Pax6*$^{Sey/+}$, the chamber angle completely vanished owing to the adhesion of the iris (Fig. 7M), and the presence of NCDCs was associated with cell accumulation and/or vessel-like structures in the vitreous body (data not shown).

The above results indicate that NCDCs contribute to various tissues in the murine eye, especially to the development of anterior segment structures, as previously shown in the chick (Hay *et al.* 1979; Johnston *et al.* 1979; Meier 1982; Nakamura 1982; Le Douarin & Kalcheim 1999) and probably to pericytes of the vitreous vessels, which were not shown in the chick (Creuzet *et al.* 2005). Importantly, *Pax6*$^{Sey/+}$ eyes show a wide range of anomalies both in the anterior segment and vitreous, in association with the aberrant distribution of NCDCs (Fig. 7O,P).

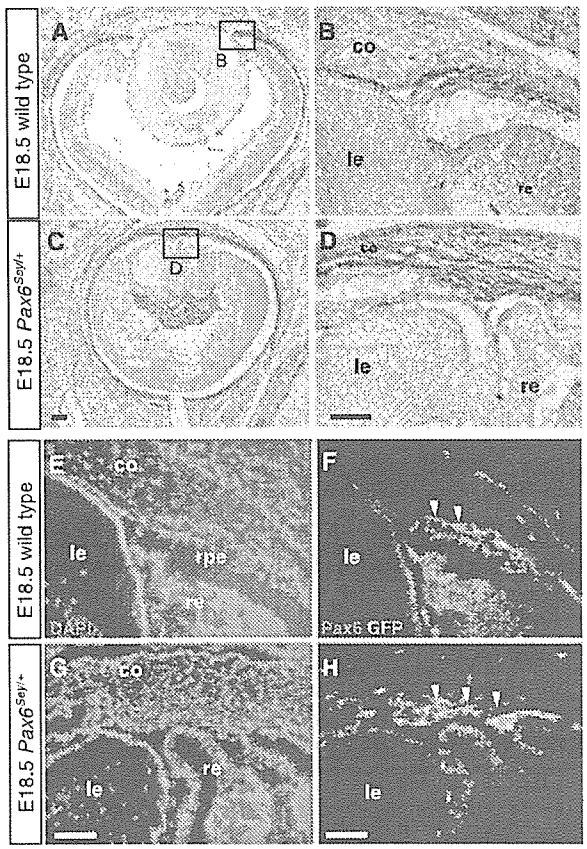

Figure 6 Abnormal development of Pax6$^{Sey/-}$ eyes is associated with NCDCs. The wild-type (A, B, E, F) and *Pax6*$^{Sey/-}$ (C, D, G, H) eyes at E18.5. (A, B) GFP-labeled cells contribute to the development of the cornea, the anterior edge of the optic cup and some cells in the vitreous cavity. le, lens; co, cornea; re, retina; rpe, retinal pigment epithelium. (C, D) In *Pax6*$^{Sey/-}$ eyes, the lens is hypoplastic, the anterior structure is obscure, and numerous GFP-labeled cells are present in the vitreous cavity. (E–H) In the wild-type, Pax6 expression (magenta) is observed in the ectoderm and optic cup (E, F), while in *Pax6*$^{Sey/-}$ eye, reduced expression of Pax6 is seen, especially in the distal part of the optic cup (G, H). GFP-labeled NCDCs (green) are observed in the corneal endothelium and adjacent to the distal optic cup in the wild-type (arrowheads in F), whereas accumulation of NCDCs is seen in *Pax6*$^{Sey/-}$ (arrowheads in H). At E18.5, GFP-labeled NCDCs never co-expressed Pax6 as seen at E10.5. Scale bars, 100 μm.

Discussion

NCDCs contribute to the ocular and periocular tissues

One of the aims of the present study was to clarify the contribution of cranial NCCs and their derivatives in the ocular structures. It has been well known that *Wnt1-Cre* mouse can provide as a tool for marking neural crest-derived components (Danielian *et al.* 1998; Chai *et al.* 2000; Matt *et al.* 2005). It is also reported that in *Wnt1-Cre*;R26R embryos, lacZ expression is observed ectopically in the dorsal neural tube and cardiac tissue (Jiang *et al.* 2000). Meanwhile, *P0-Cre* can label migrating NCCs at stages later than 9.0 dpc after detaching from the neuroepithelium (Yamauchi *et al.* 1999). The activity of *P0* promoter was previously reported in various tissues such as dorsal root ganglia, sympathetic ganglia, melanocytes, and craniofacial mesenchyme (Hasegawa *et al.* 2002; Tomita *et al.* 2005; Yamazaki *et al.* 2005). We were able to analyze the expression pattern of reporter genes driven by Cre in CD-1 background (albino color) by virtue of eliminated iris pigmentation. NCDCs were identified as the same pattern as in the C57/B6J background (black color) when the *P0-Cre* line crossed the *CAG-CAT-Z* or *CAT-CAT-EGFP* line, although the expression pattern was altered in *HTPA-Cre* mice, showing an unexpectedly leaky expression pattern (data not shown). We proved for the first time the specificity of *P0-Cre* as a genetic marker for NCC through direct DiI labeling in *P0-Cre*; GFP transgenic embryos in whole embryo culture. Thus, the *P0-Cre* reporter system seems to be adequate for genetic marking of the NCCs.

Matt *et al.* (2005) reported distribution of *Wnt1-Cre*-labeled NCDCs in the periocular mesenchyme. In the present study, we found a broad contribution of NCCs to the tissues in the anterior eye segment, such as the endothelium and stroma of the cornea and also the stroma of the iris, the wall of Schlemm's canal and ciliary body (Fig. 7O,P). In the posterior segment, NCCs also contributed to the sclera and choroidal tissues in both embryonic and adult eyes. These findings are consistent with the results shown by quail-chick chimeras (Creuzet *et al.* 2005). We also demonstrated existence of NCDCs in the vitreous cavity (Fig. 6A). Considering that cephalic neural crest provides pericytes to all blood vessels of the face and forebrain (Etchevers *et al.* 2001; Korn *et al.* 2002), these NCDCs in the vitreous cavity are likely to give rise to pericytes of the vitreous vessels, which has not been reported in the chick eye since it lacks vessel structures in the vitreous cavity.

Previous studies by DiI labeling have revealed the contribution of both midbrain and forebrain-derived NCCs to the periocular mesenchyme (Serbedzija *et al.* 1992; Osumi-Yamashita *et al.* 1994; Trainor & Tam 1995). In this study, we further found that the midbrain NCCs predominantly penetrated into the prospective vitreous cavity and the space between the lens and surface ectoderm by labeling periocular mesenchyme at the temporal side

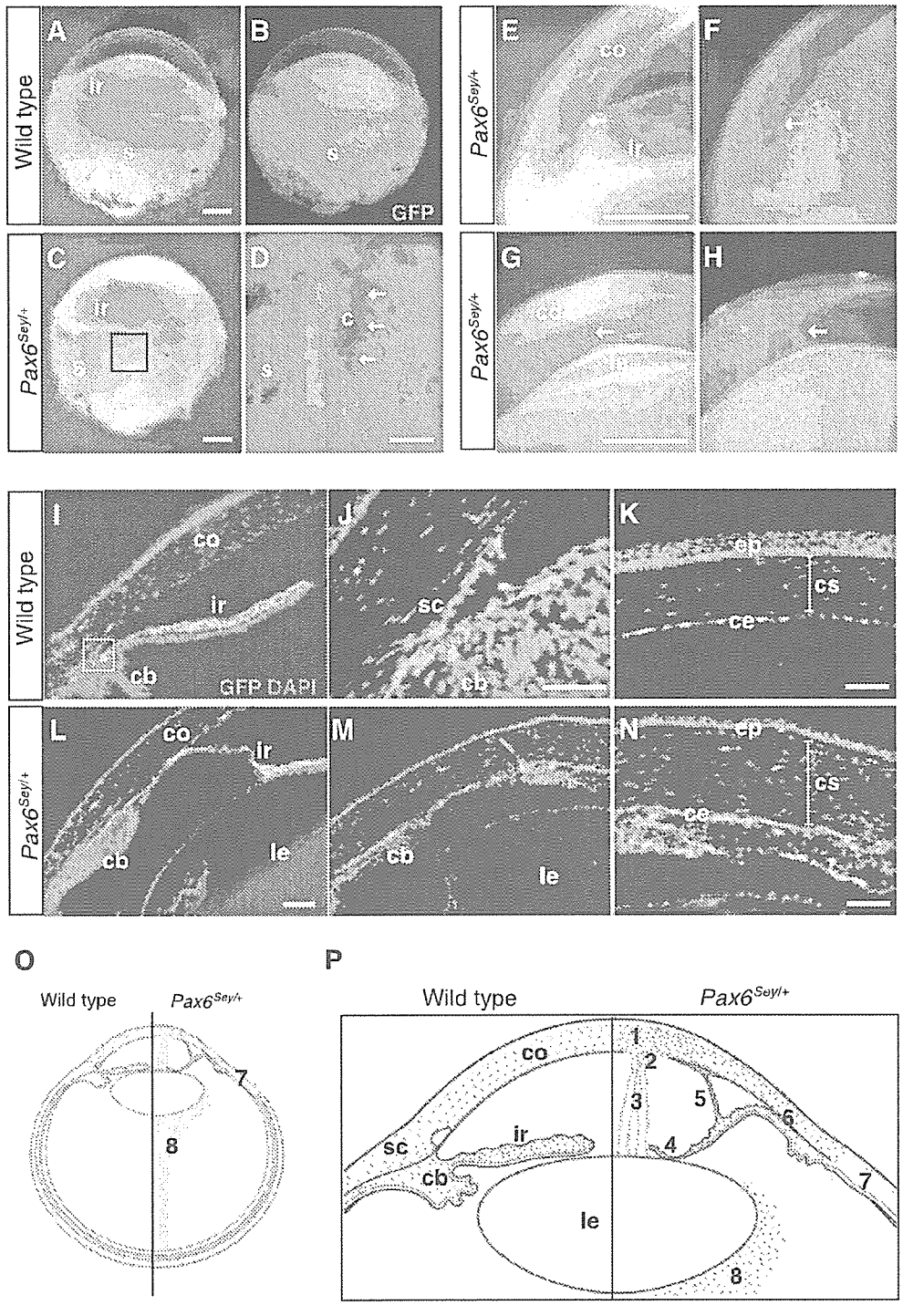

at E10.0 (Fig. 4C,G). Thus, it is reasonably assumed that midbrain crest cells are the major contributors in ocular morphogenesis.

Ocular anomalies in Small eye mouse in comparison to human eye diseases

In humans, heterozygous mutations in the *PAX6* gene have been detected in various ocular anomalies, including aniridia, Peters anomaly, autosomal dominant keratitis, isolated foveal hypoplasia and optic nerve malformations (Hanson *et al.* 1994; Prosser & van Heyningen 1998; Azuma *et al.* 2003). The present study also demonstrates a variety of comparable eye defects in *Pax6*$^{Sey/+}$ mice, especially in the anterior eye segment as compared to the retina (Fig. 7O,P). Individual eyes showed large variation in size with smaller ones showing more severe phenotypes, whereas corneal defects were quite common. All of *Pax6*$^{Sey/+}$ eyes showed corneal opacity, which may correspond to the human aniridia-related keratopathy (Mirzayans *et al.* 1995; Ramaesh *et al.* 2003). Thus, the ocular tissues derived from the mesenchyme seem to be more vulnerable to the loss of *PAX6/Pax6* function than the lens, neural retina and retinal pigment epithelium.

Figure 7 Defects in the adult *Pax6*$^{Sey/-}$ eye correlate with abnormal distribution of NCDCs. (A–H) The eyes of *P0-Cre*; *CAG-CAT-EGFP* mice at 6 weeks. Wild-type eyes (A, B) show a uniform distribution of GFP-labeled cells in the iris (ir), sclera (s) and choroid. Coloboma (c) was observed in *Pax6*$^{Sey/-}$ eyes, representing the lack of the iris and choroid associated with reduced GFP expression (arrows in D). Irido-corneal synechia (arrow in E) and keratolenticular strands (arrow in G) are frequently seen in *Pax6*$^{Sey/-}$ eyes, in conjunction with accumulation of GFP-labeled cells (F, H). (I–N) Detailed distribution patterns of GFP-labeled cells in the eye tissue. In the wild-type (I–K), GFP-labeled cells are observed in the iris stroma (ir), ciliary body (cb), Schlemm's canal wall (sc), corneal stroma (cs) and corneal endothelium (ce). J is a high magnification image of the boxed area in I, which indicates the angle structure. In *Pax6*$^{Sey/-}$ eyes (L–N), the iris and ciliary body are hypoplastic, and less GFP-labeled cells are identified in these tissues. In severe *Pax6*$^{Sey/-}$ cases, the iris adheres to the cornea and lens (L), and the angle structure is totally lost (M). Although the cornea is developed in *Pax6*$^{Sey/-}$, its epithelium (ep) is thin and the stroma shows an irregular structure (N) compared with the organized three-layer cornea of the wild-type (K). (O, P) Schematic illustrations summarizing the contribution of NCDCs in the ocular tissues of the wild-type and *Pax6*$^{Sey/-}$ mice: 1, corneal opacity; 2, endothelium defect; 3, keratolenticular strand; 4, irido-lenticular synechia: 5–6, irido-corneal synechia; 7, coloboma; 8, cell accumulation in vitreous cavity. Scale bars (A–H) 500 μm; (I–N) 100 μm.

Previous studies suggested that the corneal lesion in human aniridia is initially marked by the ingrowth of vessels from the limbal region into the peripheral cornea (Collinson *et al.* 2004; Ramaesh *et al.* 2005). Our results showed that the severity of corneal opacity was proportional to the degree of peripheral vascularization (Fig. 1A), as often observed in patients (Mackman *et al.* 1979; Nishida *et al.* 1995). Some *Pax6*$^{Sey/+}$ eyes showed corneal endothelial defect with incomplete separation of the lens, a feature that characterizes Peters anomaly in human (Kenyon 1975; Hanson *et al.* 1994). The defects in the chamber angle of *Pax6*$^{Sey/+}$ eyes were associated with the hypoplastic structure of the ciliary body and the iris, the latter often broadly adhered to the cornea. These anterior anomalies could cause glaucoma due to increased intraocular pressure because of defective Schlemm's canal that forms the major drainage pathway of aqueous humor (Grant & Walton 1974). Smaller *Pax6*$^{Sey/+}$ eyes exhibited a stalk-like cell aggregation linking the optic nerve to the posterior lens (Fig. 1A, *Pax6*$^{Sey/+}$ no. 4). This is a novel finding in *Pax6*$^{Sey/+}$ phenotypes and is considered equivalent to the persistent hyperplastic primary vitreous in human patients with mutations in *PAX6* (Azuma *et al.* 2003). These phenotypic similarities between patients with mutations of *PAX6* and *Pax6*$^{Sey/+}$ mutant mice further support the importance of *Pax6* in eye development.

Abnormal distribution of NCCs causes various small eye phenotypes

In *Pax6*$^{Sey/+}$ embryos, morphological differences were observed as early as E11.5, at the time of incomplete lens separation from the surface ectoderm. At the same time, numerous NCDCs were observed between the surface ectoderm and the optic cup as well as in the vitreous cavity of the *Pax6*$^{Sey/+}$ eye. Accumulated NCDCs in the vitreous cavity transiently contribute to the vitreous vessel in normal development. However, NCDCs further remained in a third of *Pax6*$^{Sey/+}$ adult eye, which is regarded to correspond to the hyperplastic primary vitreous of human. In *Pax6*$^{Sey/+}$, the lens is often smaller and incompletely separated from the surface ectoderm, thereby causing a wider space between the lens and the optic cup. This may eventually cause the massive influx of the NCCs from the temporal side of the periocular region into these intraocular areas. That is, some of the ocular phenotypes in *Pax6*$^{Sey/+}$ may be caused by the abnormal accumulation and distribution of NCDCs in early developmental stages.

A recent study by Matt *et al.* (2005) also reports involvement of NCDCs in eye development. They found that mice deficient for *RALDH1/3* genes encoding

enzymes for retinoic acid (RA) synthesis show ocular abnormalities such as accumulation of NCDCs in the vitreous. The RA-synthesizing enzymes are expressed in the retina and corneal ectoderm but not in the neural crest-derived periocular mesenchyme. RA produced in the retina and ectoderm is released into the ocular mesenchyme, thereby regulating eye morphogenesis. We have previously shown that expression of *RADH1* and *RADH3* are down-regulated in the *Pax6* homozygous mutant rat embryo (Suzuki *et al.* 2000). Thus, a part of $Pax6^{Sey/+}$ phenotypes can also be explained by abnormal RA-signaling in the periocular mesenchyme containing NCCs. However, the defect of *RALDH1/3* null mice is milder compared with $Pax6^{Sey/+}$ phenotypes, implying that more complicate mechanisms underlie hypoplasia of the $Pax6^{Sey/+}$ eye.

The anterior structures of the eye is extremely complicated, and develop particularly from the late embryonic to the postnatal stages in mice (Baulmann *et al.* 2002; Cvekl & Tamm 2004). We have shown here that the iris and corneal tissues contain a large number of NCDCs in the wild-type eyes, while in the adult $Pax6^{Sey/+}$ eyes, these tissues were undifferentiated or hypoplastic, sometimes leading to a total loss of the anterior chamber angle. Baulmann *et al.* (2002) reported a transient expression of *lacZ* in the iris stroma of the $Pax6^{lacZ/+}$ eye. However, we did observe Pax6 protein expression in the iris pigment epithelium and the corneal epithelium, but not in the iris stroma nor in the corneal endothelium and stroma, those tissues containing a large amount of NCDCs (Fig. 6H, and data not shown). This is quite reasonable because NCDCs never express Pax6 throughout development (Fig. 3H,J). A recent study indicates that a proper *Pax6* dosage in the distal optic cup at the mid-embryonic stage is required for subsequent iris development (Davis-Silberman *et al.* 2005). We also found that Pax6 expression decreased significantly in the anterior eye structures of postnatal $Pax6^{Sey/+}$ mouse compared to that of the wild-type one (data not shown). Taken together, these results suggest that precise regulation of Pax6 protein amount in the iris pigment epithelium and the corneal epithelium is critical for proper development of the anterior structures of the eye containing the neural crest-derived mesenchyme.

Based on the aforementioned findings, we can classify the ocular defects of $Pax6^{Sey/+}$ mutant into three categories taking into consideration the expression of Pax6 and distribution of NCDCs: Pax6-autonomous defects (the lens and retina), nonautonomous defects (vitreous body), and their combinations (the cornea, iris, angle, and ciliary body). This complex mechanism of anterior eye development would explain the wide spectrum of abnormalities seen in humans and mice with *PAX6/Pax6* mutations.

Possible involvement of Pax6 downstream molecules in migration of NCCs

The Pax6 transcription factor regulates diverse developmental processes in craniofacial and ocular morphogenesis. As for the migration of NCCs, we previously reported that homozygous *Pax6* mutant rats show craniofacial defects due to impaired migration of midbrain crest cells into the nasal region (Matsuo *et al.* 1993; Osumi-Yamashita *et al.* 1997). In the present study, $Pax6^{Sey/+}$ embryos showed altered distribution of NCDCs in the eye and lateral nasal prominence; GFP-labeled NCDCs in $Pax6^{Sey/+}$ were significantly increased in the temporal side of the eye, the site of midbrain crest cell contribution. The measurement of BrdU-incorporated NCDCs indicated that it was not due to the cell proliferation but could be caused by the different migration pattern (Fig. 5D,E). This suggests that the unbalanced distribution of NCDCs in $Pax6^{Sey/+}$ mice may be led by abnormal migration as observed in *Pax6* mutant rats. Since migrating NCDCs never expressed *Pax6*, it is regarded that the defective migration of NCCs in $Pax6^{Sey/+}$ mouse is a non-cell autonomous effect of *Pax6* haploinsufficiency.

In the *Pax6* homozygous mutant rat, midbrain NCCs accumulate in the dorsal side of eye primordium due to ectopically localized HNK-1 epitope in the frontnasal ectoderm under which NCCs migrate (Nagase *et al.* 2001). The *GlcAT-P* gene encoding an enzyme for the synthesis of HNK-1 carbohydrate epitope is ectopically up-regulated in the frontonasal ectoderm (i.e. *Pax6-expressing tissue*) including the future lens and corneal epithelium. Taking account of *in vitro* experiments, HNK-1 carbohydrate seems to be functional in repelling NCCs to migrate into the nasal region. In the mouse, however, we could not observe altered expression of HNK-1 epitope in the head ectoderm of the wild-type and $Pax6^{Sey/+}$ embryos (data not shown). Such a species-specific regulation of downstream gene expression by Pax6 was previously reported (Arai *et al.* 2005). The HNK-1 epitope is often found on various cell adhesion molecules (CAM) and extracellular matrix, and it has been reported that Pax6 controls expression of genes related with cell-cell and cell-substrate interactions (Chauhan *et al.* 2002). We checked the expression of several candidate molecules including NCAM, L1 and β-integrin both in the wild-type and $Pax6^{Sey/+}$, but no difference was observed (data not shown).